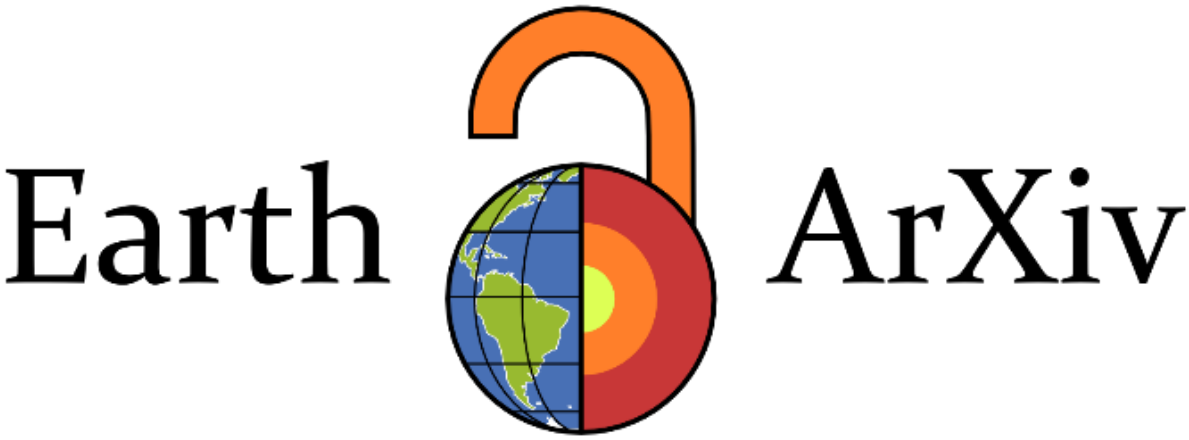


Peer review status:

This is a non-peer-reviewed preprint submitted to EarthArXiv.

A new approach to the retrieval of Land Surface Temperature and Emissivity from multi-channel instruments: an Optimal Estimation methodology for the ASTER instrument.

Mike J. S. Perry[1, 2], John J. Remedios[1, 2], Darren J. Ghent[1, 2], Karen Veal[1, 2], Frank Göttsche[3], Ben Courtier[1,2]

[1]Earth Observation Science, School of Physics and Astronomy, University of Leicester, UK

[2]National Centre for Earth Observation, Space Park Leicester, University of Leicester, UK.

[3]Karlsruhe Institute of Technology., Germany

Mike Perry (mike.perry@leicester.ac.uk)

Key Points:

- A new optimal estimation algorithm retrieves land surface temperature, spectral emissivity and total column water vapour from high-resolution ASTER thermal infrared observations.
- The method works directly with top-of-atmosphere brightness temperatures and provides traceable per-pixel uncertainty estimates.
- Simulation, in-situ validation, and MOD21 intercomparison support the retrieval of land-surface temperature and emissivity across diverse land-surface conditions.

Abstract

With increasing demand for higher-spatial-resolution land surface temperature (LST) data, there is a need to characterise the thermal land surface in terms of both LST and land surface emissivity (LSE). This paper presents the first optimal estimation retrieval of LST and LSE from high-spatial-resolution, multi-band thermal infrared observations, demonstrated using the five-channel ASTER instrument at 90 m spatial resolution. The method works directly with top-of-atmosphere brightness temperatures and retrieves LST, multispectral LSE, and total column water vapour simultaneously, while providing traceable per-pixel uncertainty estimates. In simulations using laboratory-based emissivity databases and reference geophysical scenarios, the algorithm retrieves LST to 1.5 K or better with a median LSE error of 0.01; uncertainties per pixel are 1.43 K for LST and 0.016 for LSE on average. Validation against in situ measurements results in biases of less than 1 K, and intercomparison with the MODIS MOD21 product results in an overall bias of -0.22 K. LSE absolute biases between MOD21 band 31 and ASTER channel 13 are 0.01 to 0.02, depending on site. The new optimal estimation approach confirms the capability of multi-band sensors to derive LSE with quantified uncertainty and provides improved emissivity information for energy-budget and flux models from local to global scales.

1. Introduction

The land surface temperature (LST) variable describes the radiative temperature at the surface-air boundary and has a coupled relationship with many of the significant surface energy fluxes. Furthermore, it is a key input to the understanding of vegetation health and productivity through monitoring of heat stress (Kestens *et al.*, 2011) and evapotranspiration (Delogu *et al.*, 2021) which is important for food security. High resolution LST is an area of increasing interest at both a scientific (Xue *et al.*, 2020; Firozjaei, Kiavarz and Alavipanah, 2022; Li *et al.*, 2023) and user level (Hulley *et al.*, 2019; Rangisetty *et al.*, 2020; Shi and Hu, 2021). It is a key component of studies into the urban heat island (UHI) (Badarinath, Chand, Madhavilatha, & Raghavaswamy, 2005) and a key parameter for integration into surface energy balance studies (Friedl, 2002; Voogt and Oke, 2003). As the surface energy balance describes the balance of energy fluxes through the surface air boundary, one of the most important components of the energy balance is the temperature of the surface itself.

In many satellite products, LST is being derived using a single, spectral-window-channel or a split-window (SW) algorithm; while a single window retrieval assumes a pre-specified atmosphere, the split window uses differential absorption to (implicitly) estimate the atmospheric state. SW algorithms have been applied to instruments such as ATSR and MODIS (Zhengming Wan and Dozier, 1996; Justice *et al.*, 1998; Prata, 2002; Liu *et al.*, 2019). However, SW algorithms are limited by the fact that they require specific band pairs in the 11-12 μm atmospheric window and are therefore not applicable to all thermal infrared (TIR) instruments. Additionally, whilst improving atmospheric correction in comparison to single-channel methods, SW algorithms do not retrieve the surface emissivity. This makes them reliant on ancillary data for this parameter (Ghent *et al.*, 2017), a limitation that can have significant effects particularly at high resolution with heterogeneous surfaces (Sobrino *et al.*, 2016).

Many current studies use single-channel retrievals from high-spatial resolution sensors such as Landsat (Jimenez-Munoz *et al.*, 2009, 2014; Chen *et al.*, 2011). These studies provide insight into the spatial structures but derive their ancillary knowledge of the surface emissivity entirely from parameters such as the normalized difference vegetation index (NDVI) and land use/land classification (LULC) (Yuan and Bauer, 2007; Cristóbal *et al.*, 2009; Kahya, Bayram and Reis, 2010).

The retrieval of the LST alone is not sufficient to fully characterise the heterogeneous thermal land surface, observed at high spatial resolution (French *et al.*, 2008). Land surface emissivity (LSE) is required to achieve both accurate LST and to provide surface information on LULC properties at the scales of the observations (Ridd and Liu, 1998; Chen *et al.*, 2012; Hussain *et al.*, 2013). In line with previous studies and methodologies, data of climate quality should aim to retrieve to 1 K in LST (WMO *et al.*, 2022), with mean LSE uncertainty across the channels aiming for 0.015 (e.g. Hulley, Hughes and Hook, 2012b).

There are existing algorithms, such as the temperature emissivity separation algorithm (TES), that do derive both LST and LSE. The TES methodology retrieves simultaneous LST and LSE from the Advanced Spaceborne Thermal Emission and Reflection Radiometer (ASTER) TIR channels using a hybridisation of three algorithms: normalised emissivity module (NEM), the RATIO algorithm (RAT), and max-min difference (MMD). TES first applies an estimated atmospheric correction to the sensor's brightness temperatures (BTs). The LSE is then derived using a calibration curve and, the empirically derived, MMD spectral emissivity contrast to find the minimum emissivity (Gillespie *et al.*, 1999).

In simulations, TES retrieved LST to an accuracy of 1.5 K for 95% of the spectral library materials using a surface at 300 K. Although TES has been a considerable success in taking advantage of multi-band data (Hulley, Veraverbeke and Hook, 2014; Román *et al.*, 2024), there are a number of limitations with this methodology: the need to atmospherically correct data prior to input into TES; the potential inaccuracies over grey bodies with weak spectral contrast (although there have been some attempt to address this (Ermida *et al.*, 2020)); the dependence on the mix of materials in the emissivity calibration curve (Michel et al, 2021).

Optimal estimation (OE) is an inverse method that has been widely utilised in a variety of remote sensing applications, and uses both observations and prior knowledge to optimise our estimates of the retrieved quantities, in this case LST and LSE. OE has been used in sea surface temperature (SST) retrieval where emissivity is very well characterised (Merchant *et al.*, 2008, 2009; MacCallum and Merchant, 2012; Nielsen-Englyst *et al.*, 2018; Merchant, Saux-Picart and Waller, 2020). A first attempt to use these OE techniques to retrieve LST using the SW channels from AATSR (Comyn-Platt, 2013) did not result in significant improvements from LST prior estimates, probably because LSE was not included in the state vector. Kalman filters and principal component analyses have also been used for both LST and LSE retrievals for IASI and SEVIRI (Masiello and Serio, 2013; Pavelin and Candy, 2014) but these instruments are relatively coarse-scale sensors. Finally, there have been a few limited simulation studies of OE for multi-channel radiometers e.g., Matsumoto-Moriyama and Arai (1994); Liang, Wood, and Lettenmaier (1999); Liang (2001) but none of these have progressed to use with actual satellite data.

This paper describes a new application for OE, based on the methodology of Rodgers (2000), to obtain robust and accurate simultaneous LST and LSE data, which are optimised to be less reliant on spectral library material values. This is important as the pixel spectral signatures , observed by any current and projected multi-band instruments, are determined by the mean spectral mixing of the underlying spatial-emissivity structures and unlikely to match laboratory samples (Langsdale *et al.*, 2020).

The algorithm has been specifically designed to operate in the 8-13 μm range and addresses some of the issues with existing methodologies: to work directly with TOA satellite data reduce the dependence on modelled atmospheres; and retrieve LSEs that are not inextricably tied to lab-based spectra that may not represent the pixel scale surface conditions.

More generally, it will apply to any TIR scenario in which an Earth-viewing (or planetary) sensor observes the planet in multiple spectral bands or is hyperspectral, and in which reflectance or scattering of the solar downwelling flux can be neglected. The new approach is therefore significant for the upcoming tranche of thermal satellite missions for the next decade as it delivers a well-characterised thermal emissivity spectral shape at high spatial resolution, with uncertainties, and hence reduces one unknown in the retrieval of per-pixel surface temperatures which are closer to real-world; for example the Copernicus Land Surface Temperature Monitoring (LSTM) satellites. Here, the illustration is for the specific example of the past case of ASTER which has five bands; fewer channels will imply a lower information content.

The key goals of this paper are to present a novel OE approach for simultaneous retrieval of LST and LSE, assess its performance using simulated data and in situ validation, characterise its behaviour across spectrally variable surfaces, and evaluate its consistency with established satellite LST and LSE products.

2. Materials and Methods

2.1. ASTER

ASTER is a joint USA-Japanese instrument launched aboard Terra in 1999. It operates over a large wavelength range with channels in the visible near-infra-red (VNIR), the short wave infra-red (SWIR) and the TIR (Abrams, 2000). The relevant TIR channel specifications are shown in Table 1.

Channel No.	Spectral Range (μm)	Noise equivalent differential temperature	Absolute Accuracy (σ)	Spatial Resolution
10	8.125 - 8.475	≤ 0.3 K	≤ ± 3 K (200 -240 K)	90 m
11	8.475 - 8.825		≤ ± 2 K (240 -270 K)	
12	8.925 - 9.275		≤ ± 1 K (270 -340 K)	

13	10.25 - 10.95	≤ ± 2 K (340 -370 K)
14	10.95 - 11.65	

Table 1 – ASTER TIR Spectral ranges for all channels, including the design requirements for radiometric resolution and absolute accuracy (Yamaguchi *et al.*, 1998)**. Radiometric quantities are expressed as BT in units of K.**

Terra is a polar orbiting satellite with an equatorial crossing time of 10:30 am local time. It is on a cycle with a revisit time of 16 days. Data used in this study from the ASTER instrument is L1T V003 orthographically corrected data.

2.2. Optimal Estimation

The OE retrieval follows the underlying methodology of Rodgers, (2000). OE uses a prior estimate of the retrieved parameters, represented in the state vector ($\boldsymbol{x}$), to create a simulation of the instrument observations $\boldsymbol{F}(\boldsymbol{x}_a)$ and compares this simulation to the real observations ($\boldsymbol{y}$). OE iteratively works to reduce the differences between the simulations and the observations through applying Bayesian theory assuming multivariate, at least locally, Gaussian error distributions. This is achieved through modifying the state vector to improve the estimation by optimising the closeness of the estimate to the prior, balanced against simulation minus observations differences within the relative error-covariances of both the prior and observations.

The retrieved state vector is defined as: LST (T_s), LSE per band (ε_λ) and total column water vapour (TCWV), w:

$$\boldsymbol{x} = [T_s, \varepsilon_{10}, \varepsilon_{11}, \varepsilon_{12}, \varepsilon_{13}, \varepsilon_{14}, w] \qquad (1)$$

The TOA BTs are the observations:

$$\boldsymbol{y}^T = [y_{10}, y_{11}, y_{12}, y_{13}, y_{14}] \qquad (2)$$

with associated noise equivalent delta temperature (NEdT) incorporated as an error covariance of the observation ($\boldsymbol{S_y}$). The assumption that all the observation covariance comes from the NEdT is suboptimal, providing only an incomplete covariance on the retrieval. However, this has the advantage of allowing for a greater departure from the prior in retrievals, i.e. measurement sensitivity. Furthermore, evidence (Hook at al, 2007) suggests insignificant inter-channel differences from zero within bias uncertainties (0.6 K) so it would be unwise to introduce unknown inter-channel biases. Fast radiative transfer model (RTM) simulations are known to have small biases of less than 0.1 K (Embury, Merchant and Filipiak, 2012) for ASTER channels 13 and 14 but require further investigation for channels 10-12.

The prior knowledge of the state vector ($\boldsymbol{x}_a$) is constrained with an error covariance ($\boldsymbol{S}_a$) which is constructed from the uncertainty on the knowledge of the prior state variable estimates. Atmospheric parameters, other than TCWV, are included information provided to the forward model but are treated separately in the non-retrieved state vector ($\boldsymbol{x}_b$) with an associated

covariance of ($\boldsymbol{S}_b$) and their values do not change from the initial inputs. An RTM is used to simulate TOA BT, given the prior state vector $\boldsymbol{F}(\boldsymbol{x}_a)$.

The agreement between the observed TOA BTs and the simulated TOA BTs (and thereby the surface information used to generate the simulated TOA BTs) is evaluated by the cost function:

$$C = (\boldsymbol{x} - \boldsymbol{x}_a)^T \boldsymbol{S}_a^{-1} (\boldsymbol{x} - \boldsymbol{x}_a) + \big(\boldsymbol{y} - \boldsymbol{F}(\boldsymbol{x})\big)^T \boldsymbol{S}_y^{-1} \big(\boldsymbol{y} - \boldsymbol{F}(\boldsymbol{x})\big) \qquad (3)$$

In the first iteration the forward model is run for $\boldsymbol{x}_a$ and $\boldsymbol{x}_b$. This leaves only the impact of the difference between the observed and simulated BTs, modified by the observation covariance.

The OE approach allows the algorithm to improve upon the first guess surface variables. Multiple iterations are performed building upon the previous runs to reduce the residuals between the observed and simulated brightness temperatures whilst considering the closeness to the prior state through the prior error covariance. The updated retrieved state for each iteration (i) is given by:

$$\boldsymbol{x}_{i+1} = \boldsymbol{x}_i + \big(\boldsymbol{K}_i^T \boldsymbol{S}_y^{-1} \boldsymbol{K}_i + \boldsymbol{S}_a^{-1} + \gamma \boldsymbol{I}\big)^{-1} \big[\boldsymbol{K}_i^T \boldsymbol{S}_y^{-1} \big(\boldsymbol{y} - \boldsymbol{F}(\boldsymbol{x}_i)\big) - \boldsymbol{S}_a^{-1} (\boldsymbol{x}_i - \boldsymbol{x}_a)\big] \qquad (4)$$

$\boldsymbol{K_i}$ is the matrix of partial derivatives, or Jacobian, which is a change in BT due to a change in the state vector, i.e. $\partial \boldsymbol{F}(\boldsymbol{x}_i) \,/ \partial \boldsymbol{x}$ and is used in this retrieval in the form shown in equation (5) γ is the Marquart-Levenberg scaling factor and I is an identity matrix. TCWV is implemented as a multiplicative scaling of a fixed vertical water vapour profile shape.

$$\boldsymbol{K}_i = \begin{bmatrix} \partial y_{10}/\partial T_s & \partial y_{10}/\partial \varepsilon_{10} & 0 & 0 & 0 & 0 & \partial y_{10}/\partial w \\ \partial y_{11}/\partial T_s & 0 & \partial y_{11}/\partial \varepsilon_{11} & 0 & 0 & 0 & \partial y_{11}/\partial w \\ \partial y_{12}/\partial T_s & 0 & 0 & \partial y_{12}/\partial \varepsilon_{12} & 0 & 0 & \partial y_{12}/\partial w \\ \partial y_{13}/\partial T_s & 0 & 0 & 0 & \partial y_{13}/\partial \varepsilon_{13} & 0 & \partial y_{13}/\partial w \\ \partial y_{14}/\partial T_s & 0 & 0 & 0 & 0 & \partial y_{14}/\partial \varepsilon_{14} & \partial y_{14}/\partial w \end{bmatrix} \qquad (5)$$

The cost function, as shown in equation 3, returns one scalar value per iteration. For each iteration, the current value of the cost function is compared to that of the previous iteration. The increase or decrease of the cost function is evaluated to assess whether any improvement has been made in this iteration step. Using the Levenberg-Marquardt iteration (Levenberg, 1944; Marquardt, 1963) following the methodology of Press *et al.* (2007), and the updates from Fletcher (1971), if the cost function is reduced the step is "accepted" the state vector ($\boldsymbol{x}_i$) set equal to the revised estimate $\boldsymbol{x}_{i+1}$. If cost function increased or one of the vector elements become non-physical (i.e. LSE > 1) the step is "rejected" and the state vector remains unchanged, see flow in Figure 1.

The number of iterations will ideally be small where the problem is linear within the size of the uncertainties; however, it is necessary to include a maximum number of iterations. In this scheme, if a retrieval exceeded five iterations, it was classified as non-convergent and considered a failed retrieval. This limit was determined empirically through the analysis of the number of iterations used across simulated retrievals on the ECOSTRESS spectral library (Meerdink *et al.*, 2019) with ECWMF Reanalysis V5 (ERA5) atmospheres. Most retrievals converged within 3 iterations however; there were a small number of retrievals where it took up to five iterations to converge. Retrievals that took more than five iterations generally did not converge.

The relationship between the observation differences and the retrieval increment is calculated in the form of the gain matrix ($\boldsymbol{G_y}$):

$$\boldsymbol{G_y} = \left(\boldsymbol{S_a^{-1}} + \boldsymbol{K^T S_y^{-1} K}\right)^{-1} \boldsymbol{K S_y^{-1}} \qquad (6)$$

$\boldsymbol{G_y}$, $\boldsymbol{x}$ and $\boldsymbol{K}$ can be used in conjunction, to determine the sensitivity of the retrieval to the true state ($\boldsymbol{A}$) (sometimes called the averaging kernel). In an idealised retrieval, $\boldsymbol{A}$ would be close to the identity matrix:

$$\boldsymbol{A} = \boldsymbol{G_y K} \qquad (7)$$

As well as the explicit sensitivity functions, OE offers a framework for calculating uncertainties analytically. The uncertainty can be classified into distinct sources: the smoothing uncertainty, model parameter uncertainty, and the retrieval noise uncertainty. The estimated error covariance of the retrieved state is not diagonal, but the dependencies of the different components should be encapsulated by the off-diagonal elements that are propagated through from the input prior data through to the final total uncertainty.

Smoothing uncertainty ($\boldsymbol{S_s}$) represents the uncertainty due to the difference between the true state and the retrieval. For this retrieval, this term includes the uncertainty due to the retrieved LSE.

$$\boldsymbol{S_s} = (\boldsymbol{A} - \boldsymbol{I_n})\boldsymbol{S_a}(\boldsymbol{A} - \boldsymbol{I_n})^T \quad (8)$$

where $\boldsymbol{I_n}$ is the identity matrix with dimensions of 7x7 in line with the number of elements of the state vector.

Retrieval noise uncertainty ($\boldsymbol{S_m}$) contribution is the observation uncertainty transformed into state vector space:

$$\boldsymbol{S_m} = \boldsymbol{G_y S_y G_y^T} \qquad (9)$$

Model parameter uncertainty ($\boldsymbol{S_f}$) describes the uncertainty associated with differences between the non-retrieved model parameters, such as the atmospheric state (not covered by TCWV), and the ideal input estimates which would perfectly describe the system.

$$\boldsymbol{S_f} = \boldsymbol{G_y K_b S_b K_b^T G_y^T} \quad (10)$$

This quantity can be calculated through the jacobians ($\boldsymbol{K}_b$) of the input model parameters, **b** with covariance $\boldsymbol{S}_b$, included in the simulation.

The combination of these uncertainties produces the posterior error matrix, the diagonal of which is extracted and used as the uncertainty for each of the elements of the state vector. It is understood that there is significant off-diagonal information in this matrix that is not currently being utilised in assessment, and this is an avenue for further study.

In this study, this methodology has been applied to ASTER in the following manner, as outlined in Figure 1.

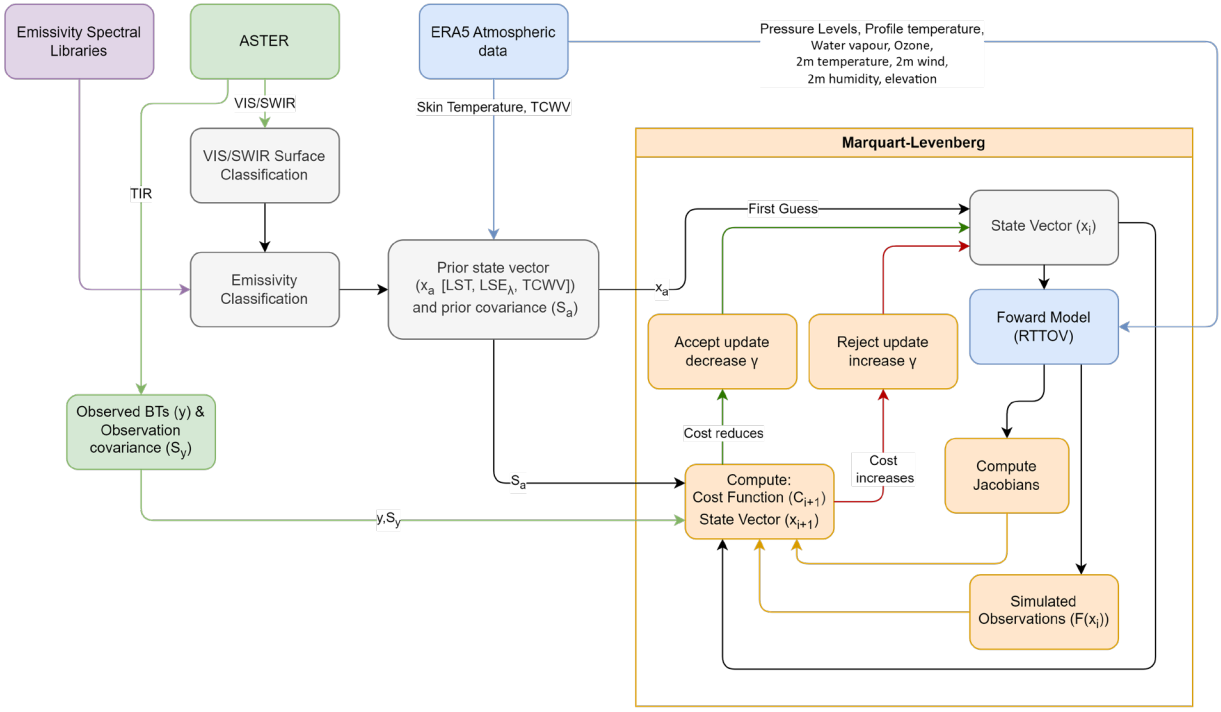


Figure 1 – Workflow for the ingestion of Input data into the OE framework and the iterative approach to arriving at the best estimate of the state vector. Accepted steps increment $\boldsymbol{x_i}$ to $\boldsymbol{x_{i+1}}$ through the update shown in equation 4.

In this study RTTOV (Radiative Transfer for TOVS) is used as the forward model. RTTOV is a fast RTM developed by the UK Met Office (Hocking, Rayer and Saunders, 2011). Built on fits to the outputs of explicit line-by-line calculations of TOA radiances, RTTOV parameterises the simulation of channel radiances, and therefore requires an Instrument Spectral Response Function (ISRF), which are used to construct pre-calculated set of coefficients relating the channel to sensitivities to various atmospheric parameters.

The RTM utilises the variables in the state vector as well as elevation, view angle, and the fixed prior atmospheric parameters: atmospheric temperature; water vapour profile shape; ozone; and the near surface atmospheric inputs of 2m temperature and humidity.

2.3 Algorithm Assessment

2.3.1 Simulation

A feature of an OE retrieval with multiple spectral bands in the TIR is the ability to estimate spectrally resolved emissivity. This provides useful data for soil fluxes and material identification and improves the estimate of the LST. To assess the OE retrieval's ability to retrieve different spectral emissivities, simulated testing was undertaken. This was to allow the largest possible range of material emissivities under comparable conditions.

Three different spectral libraries were utilised in this study. The ECOSTRESS spectral library (Meerdink *et al.*, 2019) (the successor to the ASTER spectral library) provides most of the soil and vegetation samples. The MODIS spectral library contains a mixture of urban, soil and a limited range of vegetation types. The spectral library for urban materials (SLUM) has over 70 high quality lab spectra for different urban materials broken down into ten classes (Kotthaus *et al.*, 2014). The materials have a broad range of LSEs but would all be classified into one prior LSE group within the classification methodology used here, see Figure 2.

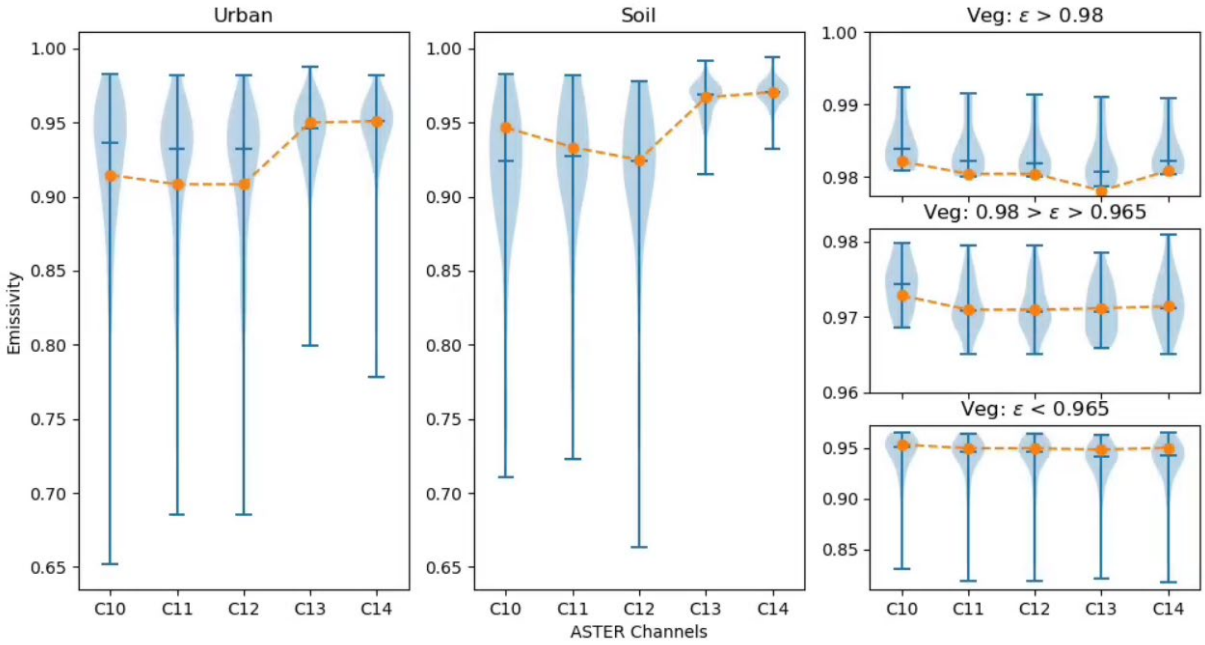


Figure 2 – The distribution of LSE values for the vegetation, urban and soil/rock classifications for the testing dataset (blue) drawn from the ECOSTRESS, SLUM and MODIS spectral libraries. The vegetation data have been split into three sets determined by the average LSE across all bands. All data have been convolved to the ASTER channels using the ISRF. The dark blue line shows the range and median of each channel, the lighter blue regions the distribution. The dashed orange line shows the values as calculated from the calibration subset to create the prior first guess.

All the materials were grouped into four categories: urban, rock/soil, vegetation, and water. However, water scenes are not retrieved in this study as the relative stability of the LSE over

water does not provide the opportunity for the most significant improvements. The vegetation category was sub-divided by emissivity as there were significant numbers of senescent materials in the ECOSTRESS spectral library. Three sub-categories were used denoting high, medium, and low emissivity. The number of materials used in the testing and training datasets from each library is shown in Table 2.

Classification	Number of materials from spectral libraries							
	Testing				Training			
	ECOSTRESS	MODIS	SLUM	Total	ECOSTRESS	MODIS	SLUM	Total
Urban	47	14	65	124	5	14	7	26
Rock/Soil	389	64	N/A	453	43	7	N/A	50
Vegetation ($\varepsilon > 0.98$)	6	3	N/A	9	1	0	N/A	1
Vegetation ($0.98 > \varepsilon > 0.965$)	43	4	N/A	47	5	0	N/A	5
Vegetation ($\varepsilon < 0.965$)	126	7	N/A	133	13	1	N/A	14

Table 2 – Number of testing and training materials used in the generation of prior LSE, LSE covariance, and the simulated testing data.

The emissivities provided by all the spectral libraries are retained at 0.01 μm spectral resolution over a large wavelength range. To obtain useful values for assessment the relevant spectra were convolved with ISRF of ASTER.

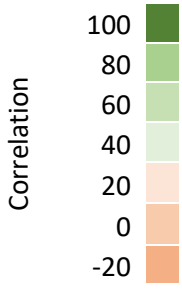
The materials in each class were split into two datasets, the testing and training. The materials in the training set were analysed in each of the three material groups to determine the LSE priors shown in Table 3. The associated prior covariance, drawn from the standard deviations of the materials within the training set, were also calculated.

Classification	Prior LSE				
	Channel 10	Channel 11	Channel 12	Channel 13	Channel 14
Urban	0.915	0.908	0.908	0.950	0.951
Rock/Soil	0.947	0.933	0.925	0.967	0.971

Vegetation (ε > 0.98)	0.982	0.980	0.980	0.978	0.981
Vegetation (0.98 > ε > 0.965)	0.973	0.971	0.971	0.971	0.971
Vegetation (ε < 0.965)	0.953	0.950	0.950	0.948	0.950
Urban uncertainty	0.042	0.051	0.052	0.037	0.024
Rock/Soil uncertainty	0.073	0.068	0.065	0.013	0.008
ALL Vegetation uncertainty	0.028	0.027	0.027	0.032	0.032

Table 3 – The prior LSE values determined from the training dataset. The prior values are the means for all samples in a class, and the uncertainty the standard deviation for each. The uncertainty for vegetation was constructed from all the vegetation materials not and not for each subset individually. Vegetation covariance was weighted by a 2x factor to account for the underrepresentation of dry samples in the training set.

LSE covariances for each combination of channels were obtained for the spectral channels of ASTER over the full range of materials in each classification. This was done to allow variations which could account for potential misclassification. Particularly notable is the high covariance between channels grouped together spectrally: TIR channels 10, 11 and 12 overlap and channels 13 and 14 overlap. This pattern of high covariance was observed for all materials in the spectral libraries. The strongest correlations for urban, soil and vegetation were selected to provide the scale of the off-diagonal prior covariance matrices, see Table 4.



Urban					
	C10	**C11**	**C12**	**C13**	**C14**
C10	1.000	0.400	0.401	-0.156	-0.163
C11	0.400	1.000	0.999	0.782	0.616
C12	0.401	0.999	1.000	0.783	0.624
C13	-0.156	0.782	0.783	1.000	0.927
C14	-0.163	0.616	0.624	0.927	1.000
Rock / Soil					
	C10	**C11**	**C12**	**C13**	**C14**
C10	1.000	0.990	0.970	0.143	0.207
C11	0.990	1.000	0.985	0.182	0.249
C12	0.970	0.985	1.000	0.314	0.345
C13	0.143	0.182	0.314	1.000	0.928
C14	0.207	0.249	0.345	0.928	1.000
Vegetation					
	C10	**C11**	**C12**	**C13**	**C14**
C10	1.000	0.987	0.987	0.978	0.980
C11	0.987	1.000	1.000	0.953	0.960
C12	0.987	1.000	1.000	0.953	0.960

C13	0.978	0.953	0.953	1.000	0.998
C14	0.980	0.960	0.960	0.998	1.000

298

299

300 **Table 4** – The correlation values derived between the ASTER TIR channels observed in the
301 spectral library.

302 To test the retrieval under realistic conditions the spectral information from the libraries were
303 combined with atmospheric profiles, and surface temperature values from a model dataset. In
304 this study the atmospheric information for both prior determination and simulation testing is
305 drawn from ERA5. The ERA5 dataset is the successor to the ERA-Interim Re-analysis dataset
306 (Hersbach *et al.*, 2023).

307 While studies have raised questions about the accuracy of the ERA 5 skin temperature product
308 (Johannsen *et al.*, 2019; Luo and Minnett, 2020), this is not seen to be an issue in this
309 methodology as we are constructing a simulated truth with material / profile combinations that
310 likely would not be seen in real observations, rather we are testing a large set of emissivities
311 requiring only a realistic difference between the prior and true profiles.

312 Each of the materials in the testing dataset were combined with 450 profiles spanning the globe
313 over major land bodies and selected from 4 different times covering: summer, autumn, winter,
314 and spring, see Figure 3. This results in 343308 profile material combinations to test with.

315 The profile selection was made by dividing ERA5 data into 10° grid cells over land. Within each
316 of these cells, a single profile was selected as the truth data, and the median of all profiles in the
317 cell was used as the prior. As figure 3 shows, this allows the prior to be still geographically
318 located with the truth, but supplies significant bias between the prior and true values to provide a
319 range of conditions with which to test the algorithm, see Figure 3. Based on deviations seen in
320 the grid cells the prior LST uncertainty was set to 5 K.

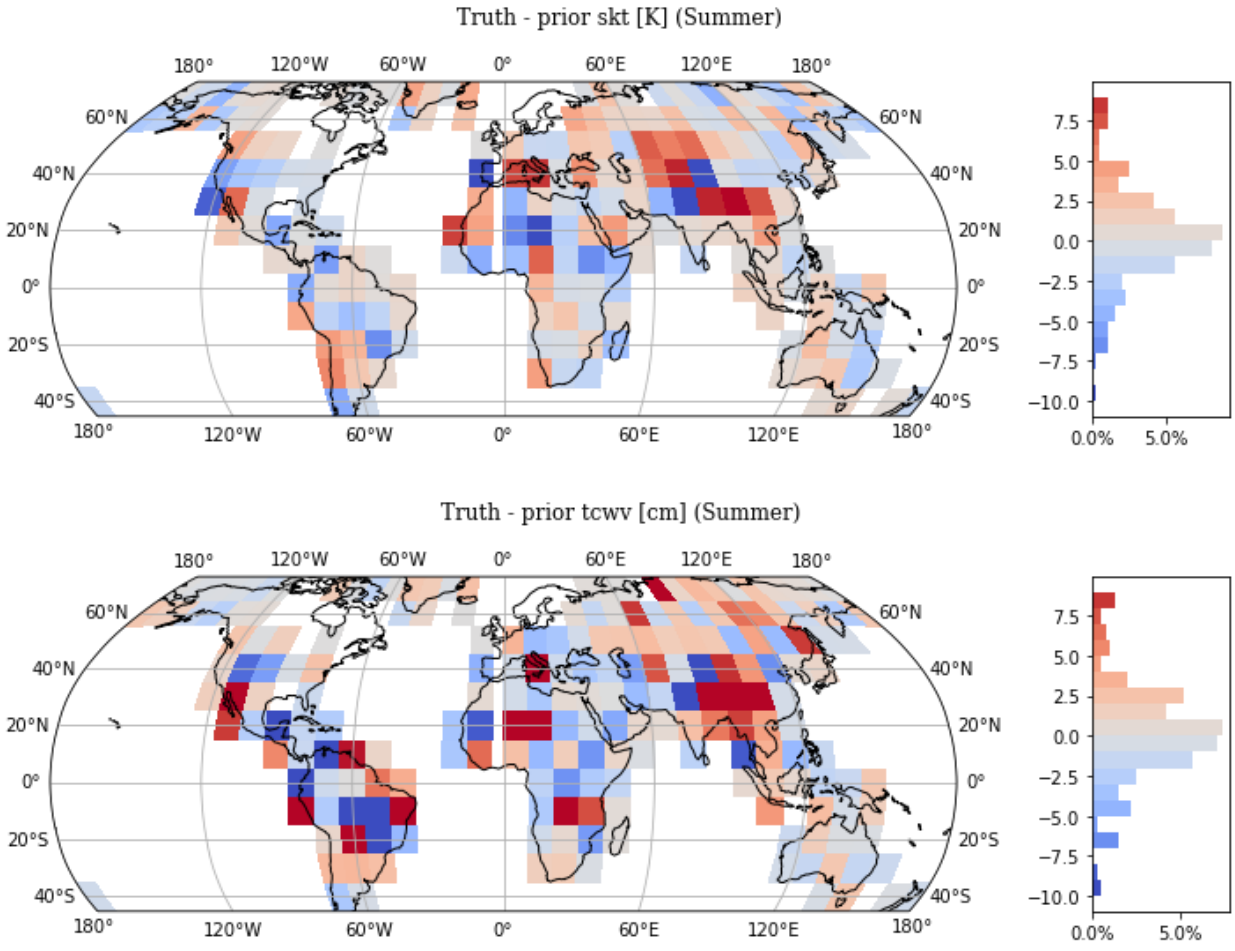


Figure 3 – Examples of Skin Temperature (Top) and TCWV (Bottom) differences between Truth and prior for the summer subset of the profiles used in the simulation. Colour bar to the right of each plot also shows the distribution of values.

Each of the LSE material-atmospheric profile combinations was put through a forward model to generate TOA BTs to simulate the satellite observations. Gaussian-distributed noise within the NEdT was added independently to each channel.

2.3.2 Validation Against In-Situ Data

In-situ validation is a critical tool to evaluate the performance of LST algorithms. In this study, we use a validation site in Gobabeb with extensive heritage in satellite LST validation (Coll *et al.*, 2005; Goettsche *et al.*, 2013; Goettsche, Olesen and Bork-Unkelbach, 2015; Duan *et al.*, 2019). The data used has been supplied by the Karlsruhe Institute of Technology (KIT) from the

GBB_Wind site [-23.55 Latitude, 15.05 Longitude]. The GBB_Wind site is located on the large and homogeneous gravel plains of the Namib Desert at 405 m above sea level in Namibia (Göttsche *et al.*, 2016) and typically has little atmospheric water vapour. Performing measurements along a 40 km track, Göttsche et.al (2012) showed that the station LST is representative for an area of several 100 km^2. A detailed assessment of the site and the surface conditions surrounding it is given in Masiello *et al.*, (2018). A full description of the in-situ observations can also be found in Göttsche *et al.*, (2017).

ASTER L1T V003 data were processed in this in-situ validation. This product is radiometrically calibrated and geo-registered with scaled radiances. The observation TOA BTs are drawn from this ASTER instrument data, the prior LSE uses the bare soil prior LSE values and uncertainties derived from the spectral libraries (see Section 2.3.1), based on the site description in Goettsche, Olesen and Bork-Unkelbach, (2015). The prior LSTs are the ERA5 skin temperatures, and the atmospheric data (including TCWV) are from the ERA5 dataset.

The OE retrieval was applied to all cloud-free matchups between the ASTER data and the GBB_Wind site over a period spanning 10 years. Matchups are allowed only within a temporal coincidence of ±5 minutes. The operational cloud-flag was used to filter for cloud. Since ASTER ran as a tasked instrument, the data volume is low, resulting in only 39 matchups. Due to the inaccuracies of the operational cloud mask a 3-σ Hampel filter (Hampel, 2014) was used to remove likely anomalous observations, this results in 32 observations: 10 daytime, 22 night-time.

2.3.3 Intercomparison against a standard MODIS LST dataset at validation sites

Additional verification of both the LST and LSE products have been made through intercomparison with the MOD21 product from MODIS. This product is produced at 1 km resolution using three spectral bands of MODIS in the TIR: 29, 31 and 32. This intercomparison was performed over two validation sites: Southern Great Plains (SGP) and Desert Rock (DR). The MODIS data is from the Terra satellite that also platforms ASTER making the overpasses coincident.

The SGP site is operated by the U.S. Department of Energy's Atmospheric Radiation Measurement (ARM) network, located in Oklahoma (http://www.arm.gov/sites/sgp/C). The station is in a large rural area with cattle pastures and wheat fields with the instrument located at a height of 10 m.

The DR station is operated by the SURFRAD network, located in Nevada. It was established in 1993 through the support of NOAA's Office of Global Programs and has been operational since 1995 (Yu *et al.*, 2012). The land classification of the station pixel is “Closed to open shrubland” according to the ESA CCI land classification dataset, and 20 x 20 pixels around the station also fall into this class, i.e., the area is very homogenous in terms of land cover. The SURFRAD stations have already been successfully utilised to validate satellite LST (Wang, Liang, and Meyers, 2008; Yu *et al.*, 2012; Li *et al.*, 2014).

MOD21 LST data and corresponding ASTER L1T V003 TOA BT data were obtained over both sites. The time range is from 2001 till 2008 for SGP and from 2000 till 2008 for DR. Both the MODIS and the ASTER data were extracted to match the spatial coordinates of the validation

sites. For MODIS, an exact pixel patch was used, for ASTER a 5x5 pixel area was averaged over the validation site to mitigate some of difference in scale between the sensors.

As before, the retrievals were performed with the observation TOA BTs drawn from this ASTER instrument data, the prior LSE constructed from the bare soil prior LSE values with uncertainties derived from the spectral libraries. The prior LST is drawn from ERA5 skin temperature, and the atmospheric data (including TCWV) are also drawn from the ERA5 dataset.

3. Results

3.1. Simulation

The results of the simulated testing are initially broken down into the urban, soil and vegetation testing sets. These tests are primarily to test the retrieval's ability to adapt and perform across a broad and extreme range of LSEs.

In addition to the analysis of the whole simulation dataset, 9 materials have been selected (3 urban, 3 rock/soil and 3 vegetation) to highlight the retrieval's performance over different spectral shapes, see Figure 5. These materials have not been selected as representative of each classification, but to demonstrate performance over differing spectral values and different knowledge gaps between the prior and the true state.

The urban materials (Figure 4: panels a, b & c) have a large degree of variation in the true LSE (0.85 to 0.92 in channel 10) resulting in large offsets between the prior and true values. The prior covariance is also large for these materials (see Section 2.3.1). These offsets present a challenge to the retrieval as it forces the iterations to rely less upon the prior knowledge and more on the observed BTs. For all urban materials, the prior estimate for the LSE is the same, assigned due to their classification. Whilst in these three samples the prior information is a good approximation in channels 13 and 14, there is considerable mismatch between the prior and individual true LSEs in channels 10, 11, and 12. The retrieved LSEs shows greater agreement with the true values of LSE relative to the prior. This marks a shift both to reduce the magnitude of the bias, but also to better approximate the spectral space of the material LSE. The differences between retrieved and true LSE fall within the estimated retrieval uncertainties.

The soil materials (Figure 4: panels d, e & f) show large variations in channels 10,11 and 12 but are stable in channels 13 and 14. The characteristics of the soil LSE retrievals are similar to those for the urban areas. Whilst the soil spectral shapes are more variable than for the urban cases, the retrieved LSE still matches the true spectral shapes closely. The uncertainties on the retrieved values reflect these improvements and are small.

The vegetation materials (Figure 4: panels g, h & i) show far less variation across the samples than the urban and soil cases, with spectrally flat, high values of LSE. While there are a small number of senescent vegetation samples in the dataset, their impact is statistically minor compared to the verdant vegetation samples. The reduced variability of this dataset means that the prior provides a better estimate of the true surface state than for the urban and bare soil datasets. Despite this, there is still improvement in the retrieval's estimate in most channels, with band 10 showing smaller improvement than the others. Ceanothus spinosus (Figure 4: panel g)

shows that the OE retrieval does not always captures the true LSE well, showing a significant bias, however, this bias is within the retrieved uncertainties.

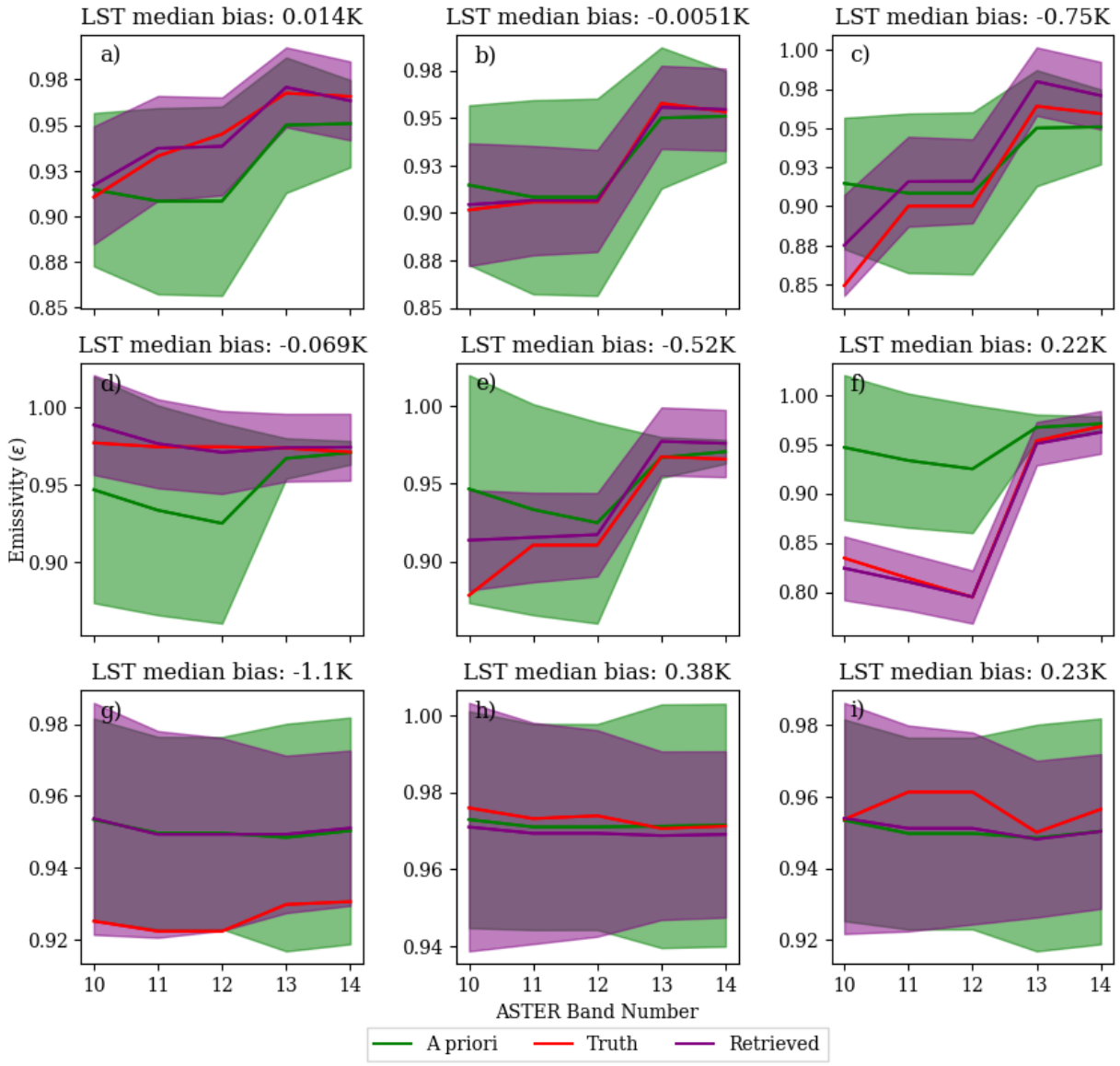


Figure 4 - Sample retrievals for the three land-cover classes. URBAN: (a) Masonry Natural from the MODIS spectral library, (b) Construction Concrete from the ECOSTRESS spectral library, and (c) Brick sample B001 from the SLUM spectral library. SOIL: (d) Brown-to-dark-brown gravelly loam from the MODIS spectral library, (e) Red-orange sandy soil from the MODIS spectral library, and (f) Sand Sample 1 from Orchard Supply Hardware in the ECOSTRESS spectral library. VEGETATION: (g) Ceanothus spinosus 1 from the ECOSTRESS spectral library, (h) Leaf of Laurel Tree (Ficus microcarpa nitida) from the MODIS spectral library, and (i) Acer pensylvanicum from the ECOSTRESS spectral library. The green curve denotes the prior land surface emissivity (LSE), with the shaded green region indicating the associated uncertainty. The red curve shows the reference (truth) LSE obtained from the spectral library. The purple curve represents the retrieved LSE, with the shaded purple region indicating the total

retrieval uncertainty. The median land surface temperature (LST) bias is reported above each panel.

There is a good agreement between the simulated and retrieved LST and LSEs across the materials, shown in Figure 5. The smallest improvements are made in channels 13 and 14, where the bias between the prior and truth is small. Deviations within the covariance of the prior can result in a poorer estimate of the truth. There are two main causes of this relationship. Only a few low LSE values in the true dataset are below 0.9 and as such are not difficult to adapt to. These points represent vegetative values that are unlikely to be seen at the satellite scale where vegetation emissivity is usually above 0.96 in the 10-12 µm range. Secondly, variation in channels 13 and 14: 0.93 and 0.96 is close to the retrieval uncertainty of 0.015.

In most cases the prior uncertainty covers the true values which could indicate an over-constraint on the prior, this does need further testing to confirm, but demonstrate the retrieval may benefit from a better constrained prior.

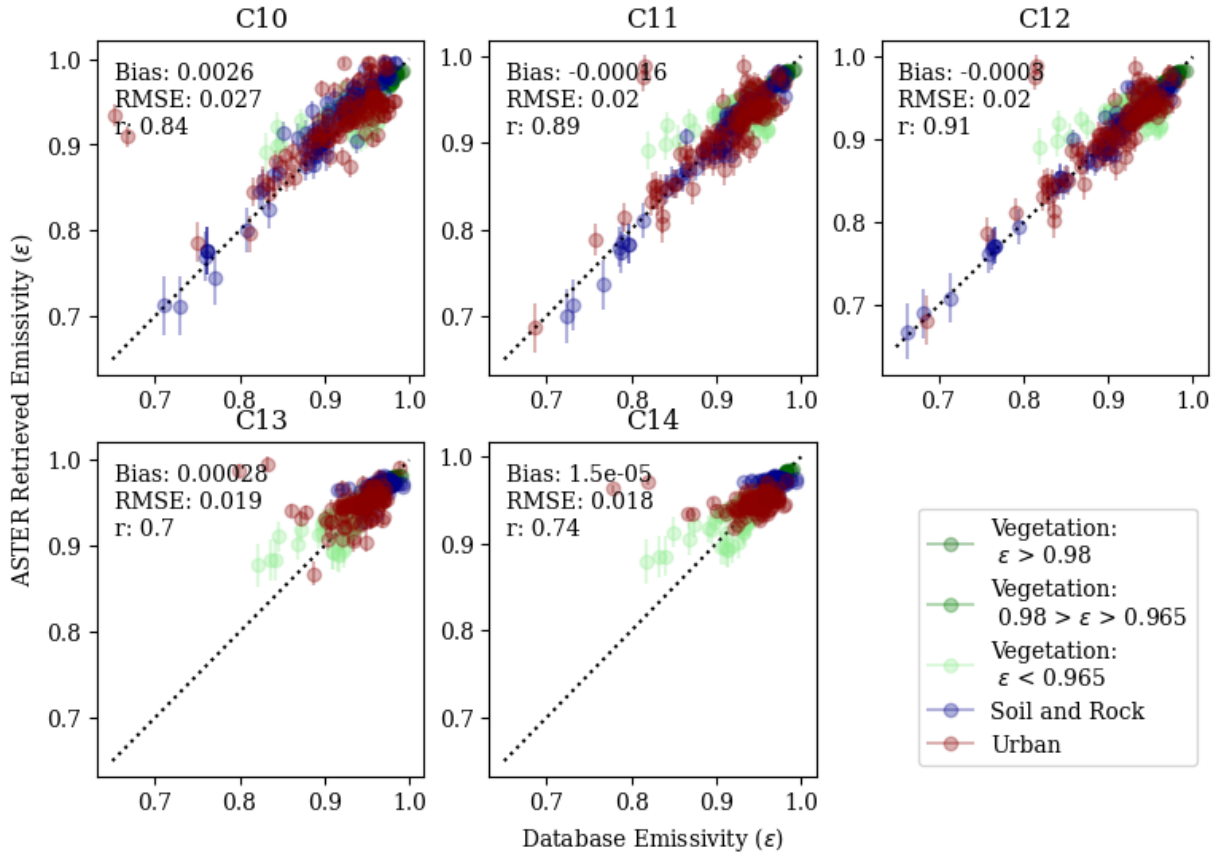


Figure 5 – Scatter plot for LSE in each of the ASTER TIR channels (10-14) comparing the retrieved and true values. Black dashed line indicates the 1:1 line. The colour of the points corresponds to the material type (outlined in the legend).

The regression coefficients for channels 10, 11 and 12, shown in Figure 5, are high, with channels 10 to 12 showing the highest consistency, particularly channel 12, and the lowest being

0.7 for channel 13. Given these correlations, and the results in Figure 4, the performance of the retrieval in this high variability test is encouraging and lends confidence to the observational retrievals of LSE. The performances in channels 13 and 14 are areas of further investigation, but the deviations from the truth are well constrained within the uncertainties. Utilising a method that accounted for both the spectrally varying values of LSE from the ASTER spectral library, and the inter-channel covariance in the prior emissivity, has given the retrieval the ability to converge to the true LSE even in cases where the true LSE is very low or significantly offset from the prior.

The LST has a median bias of –0.07 K with a standard deviation of 1.485 K, this shows a good agreement within the median retrieved uncertainty of 1.42 K. Most importantly there is significant improvement from the prior in most cases, which indicates the capability of the algorithm to adapt to real observational data, as shown in Figure 6.

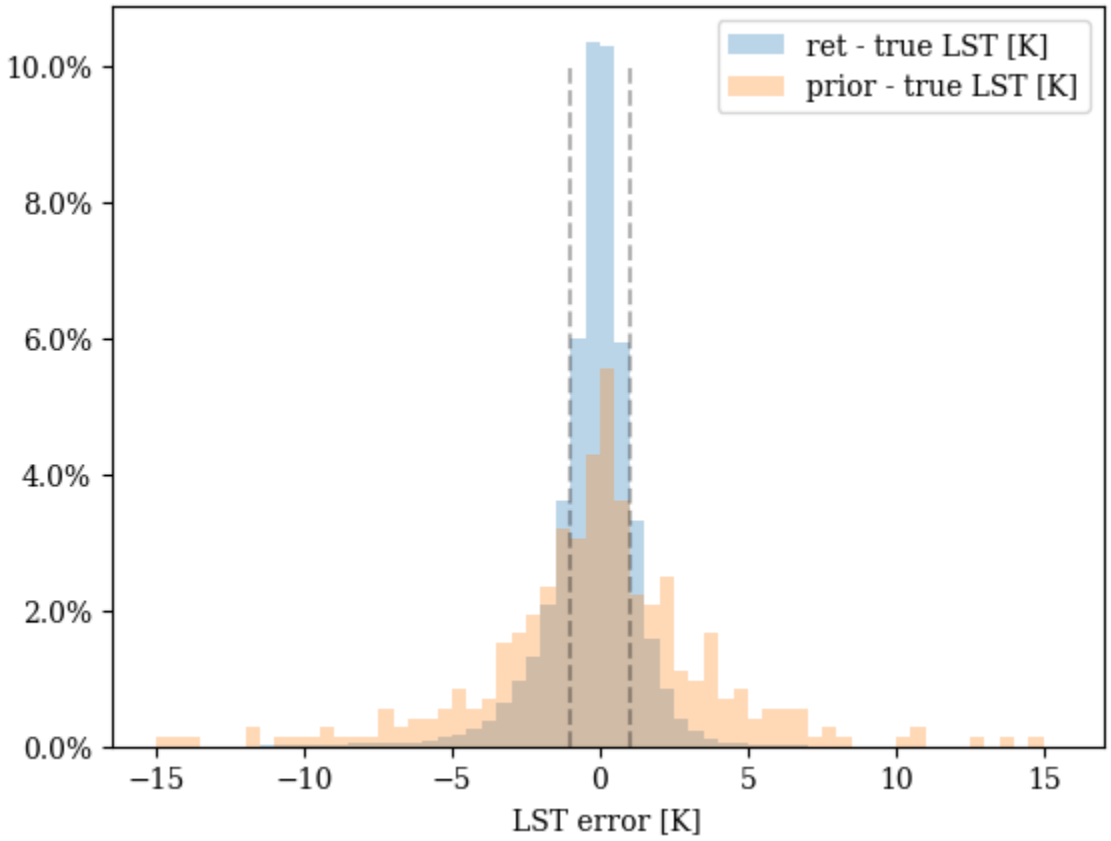


Figure 6 – Comparison of the error between the retrieved – true LST(Blue) and the prior – true LST (Orange) over all 343308 retrievals. Y-axis is shown as a percentage of all samples. Grey dashed line highlights -1 and +1 Kelvin error boundaries.

The algorithm retrieved LST to 1 K or better in 66% of the data and with 87% to within 2 K (only 53% of the prior LSTs were withing 2K of the truth), and LSEs to within 0.01. The largest biases correspond to situations where the prior LST information was significantly in error, of the order of 10 -15 kelvin, and still show a large decrease in the bias. The simulation uncertainties retrieved are better than 1 K in LST and 0.015-0.017 for LSE. This improves upon previous OE

efforts with ASTER such as Matsumoto-Moriyama and Arai, (1994) where they found that the retrieved LST, at the expected NEdT of 0.3 K, resulted in high LST errors with an RMSE of 2.23.

Furthermore, the extensive testing dataset utilised allows insight in the retrieval's performance under different conditions. Figure 7 shows that there is little bias due to changes in the surface temperature and TCWV lending weight to the algorithm's global applicability; there is a small potential increase in bias at the highest TCWV amounts.

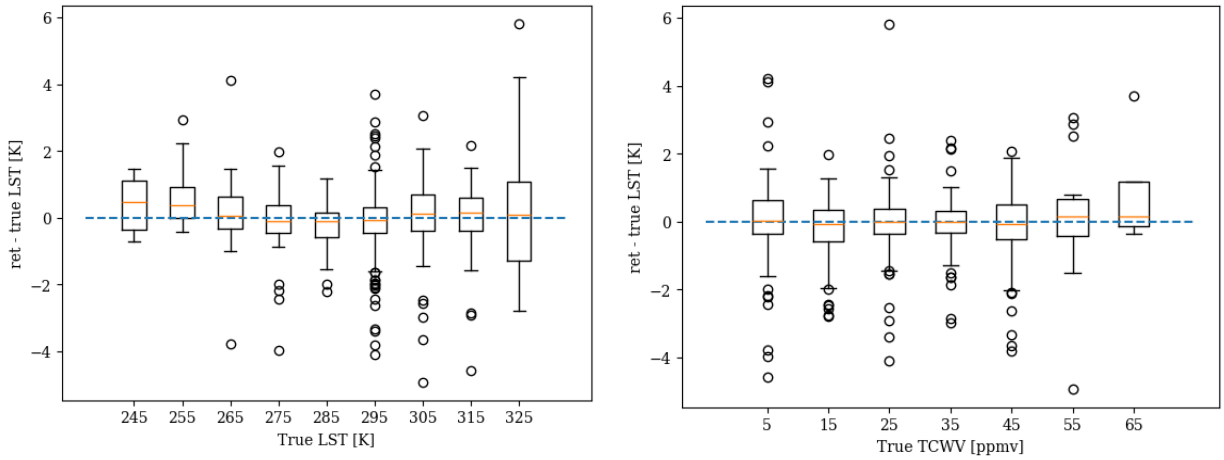


Figure 7 – Left: The retrieved – true LST [K] binned by the true surface temperature [K]. Right: The retrieved – true LST [K] binned by the true TCWV [ppmv]. The orange bar shows the median value for the bin, and the box shows the standard deviation, the whiskers denote the 95% confidence interval and the circles the anomalous points.

3.2. Validation Against In-situ Dataset

The validation regression between the OE derived LST and the in-situ LST, Figure 8, shows a good agreement with an R^2 of 0.974. There is a clear separation between the day and night data..

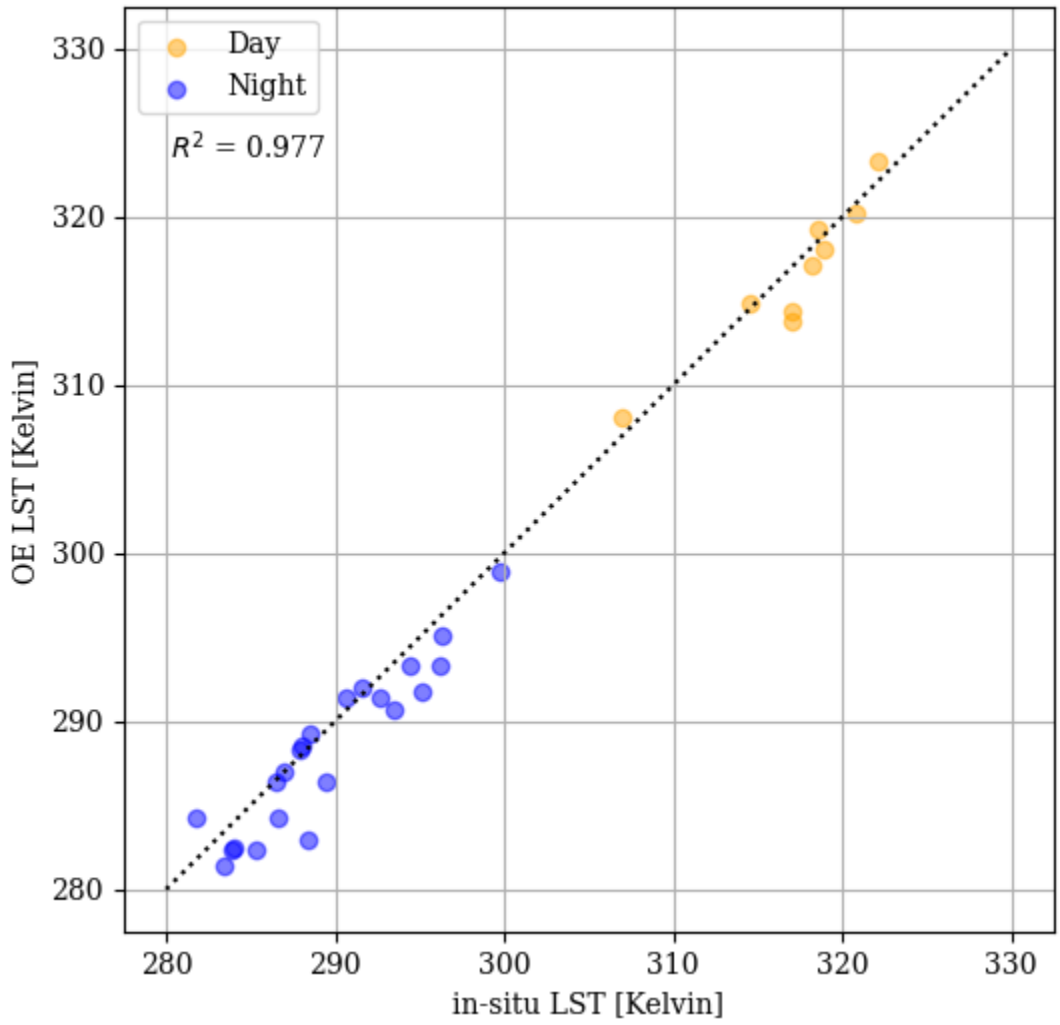


Figure 8 – Regression of the OE retrieved LST values against the in-situ LST recorded at the GBB wind station.

Furthermore, when the median values are calculated there is a very good agreement seen between the OE and the in-situ, shown in Table 5. Here the median difference is low for both the day and the night retrievals, with a smaller diffeence in the night. The mean absolute deviation (MAD) shows a similar scale of variation in day and night with a slightly larger deviation seen in the day.

	Number of scenes	Median difference (OE – In situ) (K)	MAD (K)	RMSE (K)	σ z-score
Day	9	-0.551	1.26	1.58	0.78

Night	19	-1.3	1.28	2.24	1.49

Table 5 – The number of scenes, median difference (OE – in-situ), MAD, RMSE and standard deviation of z-score for the day and night comparisons.

The OE retrieval can also be assessed against the observations. As the OE iterations attempt to estimate the surface and atmospheric conditions required to recreate the observed TOA BTs, the residual between the actual observations and the final simulated BTs can also be assessed. In an ideal retrieval the difference would be compatible within the instrument noise of up to 0.3 K The residuals are smaller the observation uncertainty suggesting possible over constraint, see Table 6.

	Median Radiance Residuals (K)				
	C10	C11	C12	C13	C14
Day	0.052	0.070	0.054	0.007	0.050
Night	0.089	0.210	0.089	0.075	0.037

Table 6 – The radiance residuals, i.e., the bias between the simulated and observed top of atmosphere brightness temperatures for the day and night comparisons.

The GBB_Wind site does not as part of its standard operation measure LSE. There have been, however, studies looking into the LSE of the site. The field study conducted by Göttsche et.al. (Göttsche *et al.*, 2017), measured LSE at several locations including at GBB_Wind with a band between 9-12 μm recording an average emissivity of 0.93 with a standard deviation of 0.016. The measurements taken on 17/06/2017 at GBB_Wind provide average LSEs of 0.84, 0.85, 0.82, 0.95 and 0.96 for Channels 10 through 14 respectively, which compare well with the in-situ assessments made in Göttsche et al (2017).

3.3. Intercomparison against a reference LST dataset

Figure 9 shows the OE retrieved LST compared to both the MOD21 and the validation dataset for SGP. Figure 10 shows the OE LST against the MOD21 data. There are some outliers where there is a difference between the retrievals, while this will require further assessment it is currently believed to be an error in the operational cloud screening where the smaller ASTER pixels are cloud contaminated by clouds too small to dominate the larger MODIS pixels.

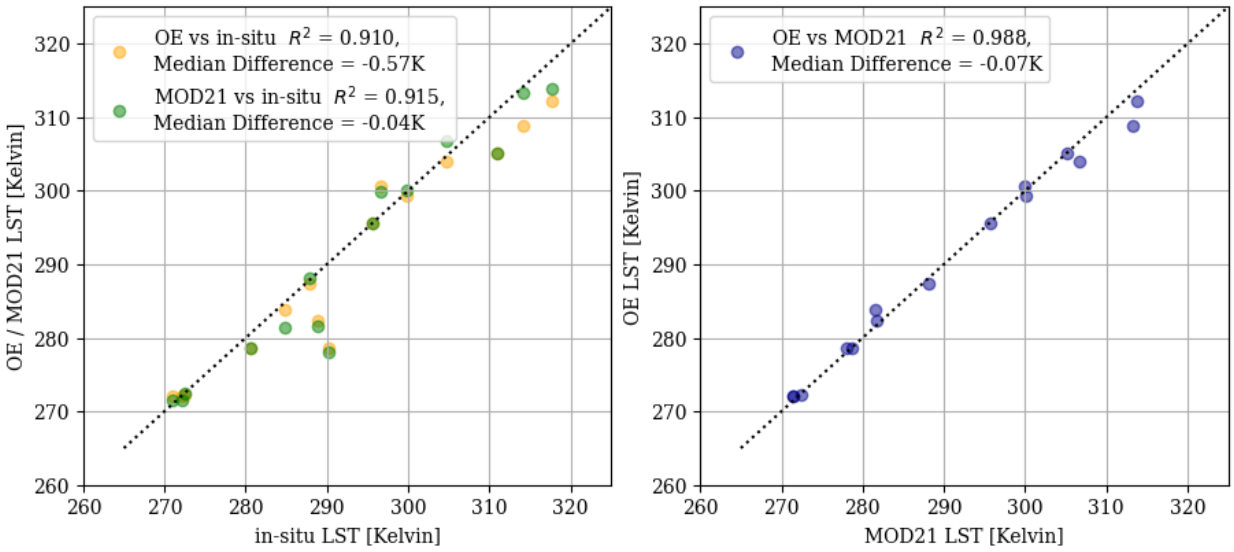


Figure 9 – Comparison of the MOD21 retrieved LST vs the OE LST retrieval (Blue), the in situ LST vs the OE retrieval (Orange) and in situ LST vs MOD21 retrieved LST (Green) over the Southern Great Plains site from 22/03/2001 till 19/11/2008.

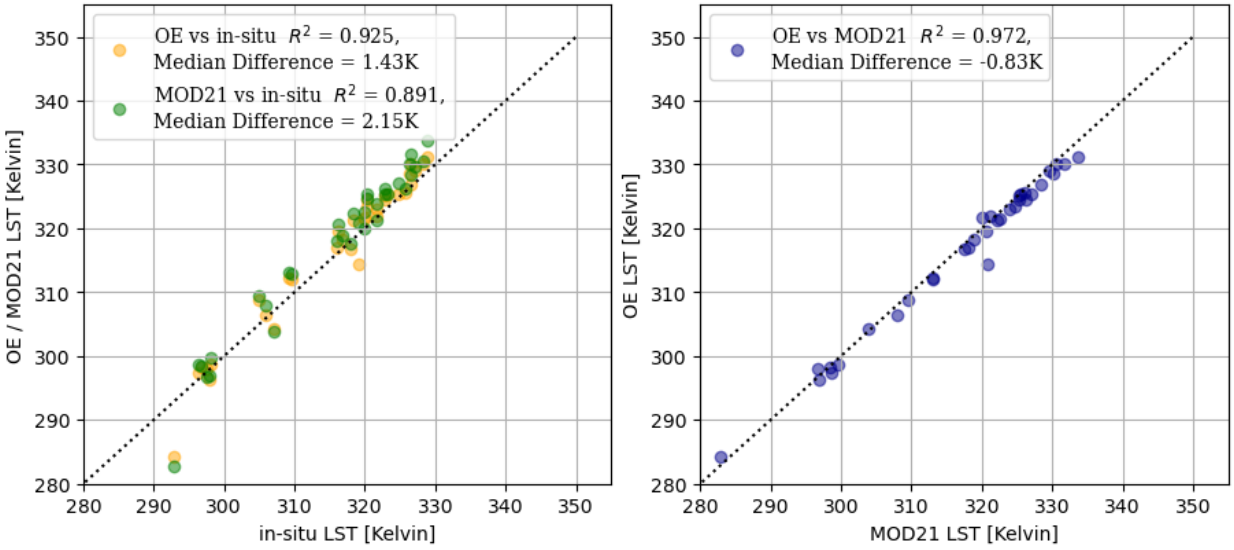


Figure 10 – Comparison of the MOD21 retrieved LST vs the OE LST retrieval (Blue), the in situ LST vs the OE retrieval (Orange) and in situ LST vs MOD21 retrieved LST (Green) over the Desert Rock site from 10/05/2000 till 21/09/2008.

The OE shows good performance for LST against the MOD21 dataset in both SGP and DR, with R^2 values of 0.988 and 0.972, respectively. The OE performs well against the SGP validation site

with an R^2 of 0.91. The median biases for the OE – MOD21 are -0.07 and -0.83K for SGP and DR, with median differences from in situ of -0.57 and 1.43K for OE - SGP and DR, respectively. There are in both OE and MOD21 outliers that are suspected to be due to cloud. Across both sites the OE retrievals with a median LST uncertainty of 1.23K.

In each of these analyses the OE LSE data was also compared to the MOD21 LSE data. The best spectral match was between ASTER band 14 and MODIS band 31 as they are both centred on the 11 µm region.

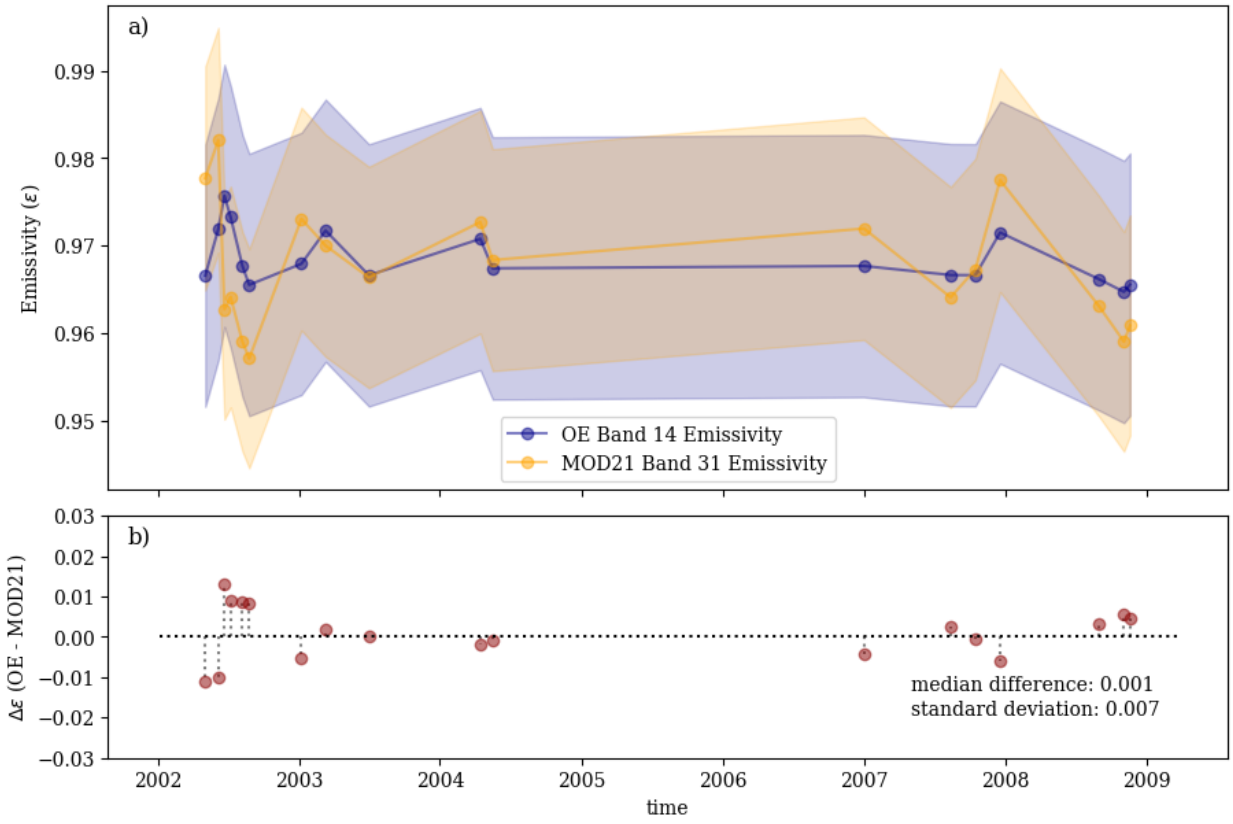


Figure 11– Difference between OE retrieved LSE (blue) and MOD21 retrieved LSE (orange) over the Southern Great Plains site from 22/03/2001 till 19/11/2008. Shaded areas denote region bounded by uncertainty for the respective retrievals.

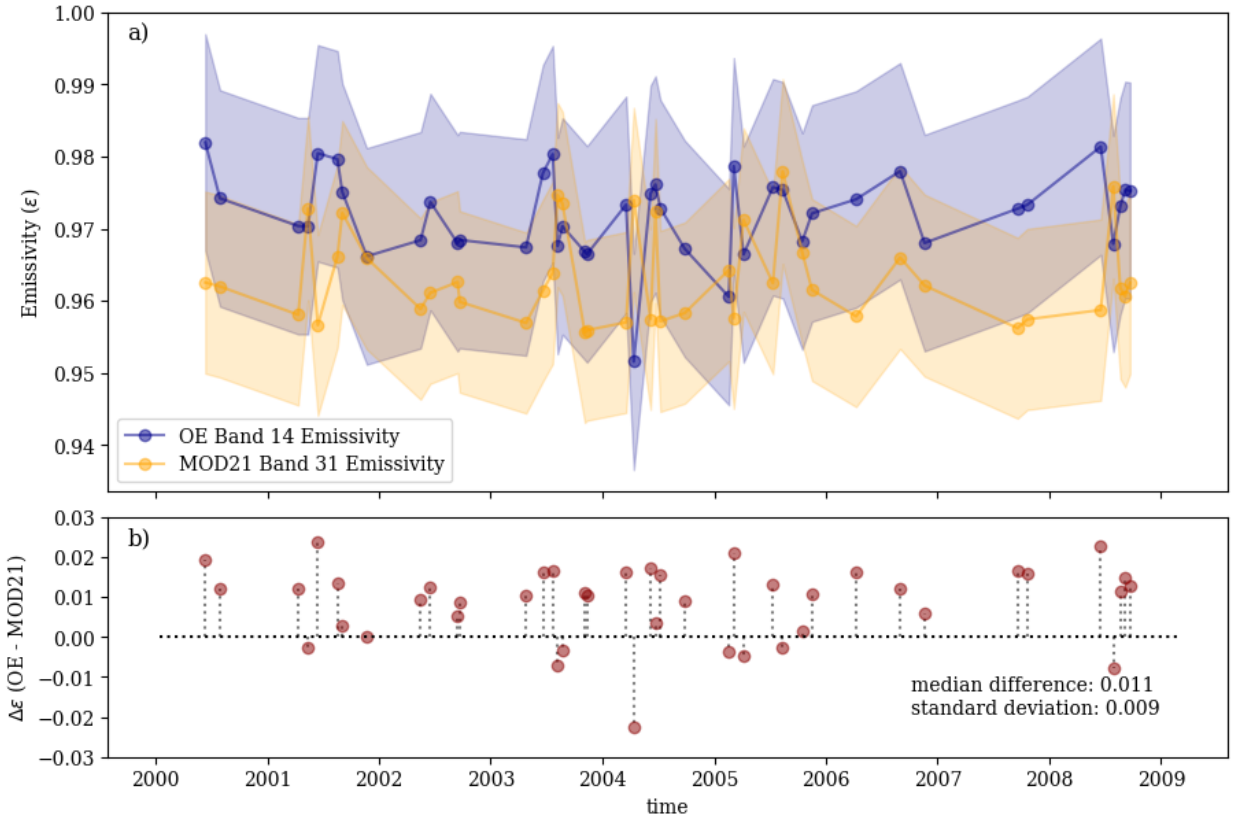


Figure 12 - Difference between OE retrieved LSE (blue) and MOD21 retrieved LSE (orange) over the Desert Rock site from 10/05/2000 till 21/09/2008. Shaded areas denote region bounded by uncertainty for the respective retrievals.

In both cases most of the match ups show good agreement within OE uncertainty; SGP provides a smaller median difference, but the differences at DR for several points are only slightly outside OE uncertainty. It is important to reiterate that this is verification, and that differences between OE and MOD21 are different from an error, due to uncertainty in the MOD21 data. The LSE associated with the SGP and DR sites is obtained from CAMEL V001 (Combined ASTER MODIS Emissivity over Land) data (Hook, 2017) using the methodology found in equation 15 of (Ghent *et al.*, 2019).

4. Discussion

The retrieval as outlined in this paper has produced the first optimal estimation retrieval of LST and LSE from ASTER data, and indeed from any high spatial resolution TIR instrument. In Section 2, a novel methodology was described that utilised the inter-channel correlations between the LSEs in the ASTER spectral library to generate prior covariance.

The methodology gave the retrieval method the adaptability to converge to close to the true LSEs across the entire range of materials tested, including simulations where the prior knowledge given to the retrieval was a poor descriptor of the true LSE, whilst maintaining an error of less than 1 K. The range of materials included many cases, such as pure quartz crystals, that are

beyond the realistic range of values that we would expect to see at the scale of a 100 m pixel, so the robustness of the retrieval under these conditions stands the retrieval in good stead for global retrievals. Testing and validation have shown that the method is robust to vegetated and bare soil areas. The algorithm has not been tested for ice/snow and specifically polar conditions where greater uncertainty in emissivity and quite variable atmosphere profiles (but low humidity) may require further characterisation. This will be a focus of further work.

The simulation results are particularly significant given the lack of site-specific emissivity information. The method optimises between the error covariance across wavelengths associated with LST uncertainty (determined by the Planck function) and the prior error covariance for the emissivity terms across wavelengths (determined from the libraries), whilst also allowing for the atmospheric TCWV to be optimised. The simulated testing against the testing materials and atmospheric profiles, resulting in uncertainties of 1.42 K and 0.01 emissivity, do seem to demonstrate an excellent performance.

The LST validation over Gobabeb provided particularly good results with biases of 0.65 and -0.26 K for the day and night, respectively. The validation focussed on the LST due to the well characterised nature and homogeneity of the site providing a stable dataset. The median retrieved uncertainties for this validation were 1.2 K at the per pixel level which is comparable with the standard ASTER TES with WVS uncertainties of 0.85-1.5 K.

However, the lack of LSE data, at this site and others, is an important blocker in the accurate validation and improvement of LST and LSE retrievals. Regular (at least seasonal) monitoring of the LSE over a site, with an emphasis of the spatial variability would be a key step forward in this area.

The verification against SGP and DR along with the intercomparison of the OE method with that of the MOD21 product showed high consistency with the existing data product, but with several key differences; OE retrieved higher values of LSE in both cases, and OE had a lower bias to in-situ over Desert Rock. The OE method is not tied to empirical look up tables and is able to retrieve estimates that are significant deviations from the prior expectation, so this range is expected, but this does represent a significant strength of the OE method in its ability to move from the first guess of the surface parameters, using the observation to move towards a better estimate. A clear limitation for quantitative data quality aspects of all these studies is the lack of rigorous, continuously monitored, site-wide in situ validation data for LSEs.

The methodology throughout this study has worked well to retrieve both LSE and LST from TOA data. The lack of reliance on prior atmospheric correction as well as the ability to react adaptively to the surface conditions as part of the retrieval process supports application across a broad range of land-surface and atmospheric conditions. Furthermore, the per pixel retrieved uncertainty is an integral part of the retrieval process meaning that all retrievals will intrinsically come with a total uncertainty for analysis and traceability.

Limitations highlighted in this study focused on the amount of information available in terms of prior classification and the number of parameters needed to be retrieved. The inclusion of the atmosphere in the retrieval process, while a significant and novel step for an ASTER retrieval, shows an uncertainty reduction of 50% from the prior which is the maximum information

extractable from the information content. Ideally, a lower uncertainty on the atmosphere uncertainties would be ideal.

5. Conclusions

This paper presents a new implementation of optimal estimation for the simultaneous retrieval of LST and LSE with traceable uncertainties. Most current methods require prior knowledge of LSE to retrieve accurate LST, which is challenging in complex landscapes. Here, we demonstrate that accurate and precise values for both LST and LSE can be retrieved using OE. The method is assessed through three approaches: simulation, in situ validation, and intercomparison with other satellite products.

The results of the simulations presented here show a retrieval capable of LST estimates to 1 K or better with LSE estimates having very low biases of 0.01. The uncertainties are also well characterised with ±1 K for LST (1 sigma) and 0.016 for LSE (1 sigma) with a range of 0.015 to 0.017. Over the homogeneous validation site of Gobabeb the OE approach resulted in biases of 0.65 K in the day and -0.26 K at night compared to in situ data, with an average uncertainty of ±1.2 K in LST. The intercomparison with the MODIS MOD21 dataset over two sites (SGP and DR) also showed very good agreement, with our results for SGP showing an improvement from MOD21 at replicating the in-situ measurements. Differences in LSE are small at SGP (less than 0.01 on average) but a little larger at DR (0.015 on average). This might be expected as the ASTER spatial resolution should in theory provide a better match to the point level validation data. However, the OE scheme could already be providing benefits in these broad sites.

The OE implementation presented in this study has several key advantages over many other approaches to retrieve LST. Firstly, its flexible methodology, due to direct ability of the fitting to invoke spectral dependence of emissivity and its use of covariance associated with material libraries, means it is not intrinsically tied to a regression of materials catalogued in spectral libraries in the manner of the TES algorithm for instance. The retrieval of LSE can reflect the spectral emissivity which is consistent with the observed multi-channel BTs. This is important for surfaces which are less well characterised in spectral libraries, such as complex vegetation. Recent research (Langsdale *et al.*, 2020, 2021) has suggested that further work is required on both reconciling field methods for emissivity in comparison to lab-based measurements, and in achieving consistent laboratory measurements. Secondly, the ability to start with TOA radiances reduces the dependence on model biases and allows the retrieval to adapt to localised changes in water vapour. Finally, this methodology has a traceable uncertainty propagation allowing analysis with associated confidence that will improve user capabilities and understanding of the LST data. Overall, our approach presents a step forward in the capabilities of climate studies around temperature, particularly with respect to complex materials spanning a broad range of spectral shapes and value ranges.

The results of our study confirm that multi-band, simultaneous, TIR observations can now offer comprehensive combined LST and LSE information with consistent atmospheric correction. The simulation results establish that the LSE information present in the ASTER channels is sufficient to achieve LST biases of less than 1 K; LSEs of 0.01 bias can be achieved. Improved LSE real-world knowledge both of laboratory spectra and of real-world land cover type would ensure that this 1 K LST bias is achieved globally; currently we believe this LST bias is achievable for many well-characterised situations but not everywhere. The new OE approach can be applied to other

existing multi-band sensors beyond ASTER such as MODIS and SEVIRI which should offer opportunities to improve the community's confidence in long-term records of emissivity as well as temperature. There are currently plans for a significant increase in thermal high spatial resolution studies with the development of Land Surface Temperature Monitoring (LSTM)(CEOS, 2024a), Surface Biology and Geology (SBG)(NASA, 2024) and Thermal infraRed Imaging Satellite for High-resolution Natural resource Assessment (TRISHNA)(CEOS, 2024b). Future LST sensors do and will benefit significantly in both design and performance from the step-change offered by this new OE implementation, particularly the Copernicus LSTM mission. Finally, improved LSE knowledge should allow updates to parameters in both global and local models of energy budgets and fluxes from the land surface interface to the atmosphere.

Acknowledgments

D. Ghent and J. Remedios have been supported by the UK Natural Environment Research Council for the National Centre for Earth Observation (grant nos. NE/R016518/1 and NE/N018079/1). M. Perry acknowledges funding from the University of Leicester for a PhD studentship and funding from the European Space Agency (contract ref. 4000140005/23/NL/SD)

Open Research

The Jupyter Notebook to execute the analysis in the paper is hosted at https://github.com/MikeJSPerry/2023EA003171R.git and is preserved at https://doi.org/10.5281/zenodo.10964924 and includes the input files needed to run the code. The data on which this article is base is the ASTER L1T V003 available at NASA LP DAAC (2021), and MOD21 L3 V061 available at Hulley, G., Hook, S. (2021).

References

CEOS (2024a) *Sentinel LSTM-A Satellite Mission Summary | CEOS Database*. Available at: https://database.eohandbook.com/database/missionsummary.aspx?missionID=1041&utm_source=eoportal&utm_content=lstm (Accessed: 2 April 2024).

CEOS (2024b) *TRISHNA Satellite Mission Summary | CEOS Database*. Available at: https://database.eohandbook.com/database/missionsummary.aspx?missionID=866&utm_source=eoportal&utm_content=trishna (Accessed: 2 April 2024).

Chen, F. *et al.* (2011) 'Retrieving land surface temperature from Landsat TM using different atmospheric products as ancillary data', *Proceedings 2011 IEEE International Conference on Spatial Data Mining and Geographical Knowledge Services*. *2011 IEEE International Conference on Spatial Data Mining and Geographical Knowledge Services (ICSDM)*, Fuzhou, China: IEEE, pp. 421–426. Available at: https://doi.org/10.1109/ICSDM.2011.5969079.

Chen, G. *et al.* (2012) 'Object-based change detection', *International Journal of Remote Sensing*, 33(14), pp. 4434–4457. Available at: https://doi.org/10.1080/01431161.2011.648285.

Coll, C. *et al.* (2005) 'Ground measurements for the validation of land surface temperatures derived from AATSR and MODIS data', *Remote Sensing of Environment*, 97(3), pp. 288–300. Available at: https://doi.org/10.1016/j.rse.2005.05.007.

686 Comyn-Platt, E. (2013) *Land Surface Temperature: A comparision of products from polar*
687 *orbiting and geostationary satellites*. Doctor of Philosophy. University of Leicester.

688 Cristóbal, J. *et al.* (2009) 'Improvements in land surface temperature retrieval from the Landsat
689 series thermal band using water vapor and air temperature', *Journal of Geophysical Research*,
690 114(D8), p. D08103. Available at: https://doi.org/10.1029/2008JD010616.

691 Delogu, E. *et al.* (2021) 'Evaluation of Multiple Methods for the Production of Continuous
692 Evapotranspiration Estimates from TIR Remote Sensing', *Remote Sensing*, 13(6), p. 1086.
693 Available at: https://doi.org/10.3390/rs13061086.

694 Duan, S.-B. *et al.* (2019) 'Validation of Collection 6 MODIS land surface temperature product
695 using in situ measurements', *Remote Sensing of Environment*, 225, pp. 16–29. Available at:
696 https://doi.org/https://doi.org/10.1016/j.rse.2019.02.020.

697 Embury, O., Merchant, C.J. and Filipiak, M.J. (2012) 'A reprocessing for climate of sea surface
698 temperature from the along-track scanning radiometers: Basis in radiative transfer', *Remote*
699 *Sensing of Environment*, 116, pp. 32–46. Available at: https://doi.org/10.1016/j.rse.2010.10.016.

700 Ermida, S.L. *et al.* (2020) 'A multi-sensor approach to retrieve emissivity angular dependence
701 over desert regions', *Remote Sensing of Environment*, 237, p. 111559. Available at:
702 https://doi.org/10.1016/j.rse.2019.111559.

703 Firozjaei, M.K., Kiavarz, M. and Alavipanah, S.K. (2022) 'Satellite-derived land surface
704 temperature spatial sharpening: A comprehensive review on current status and perspectives',
705 *European Journal of Remote Sensing*, 55(1), pp. 644–664. Available at:
706 https://doi.org/10.1080/22797254.2022.2144764.

707 Fletcher, R. (1971) 'MODIFIED MARQUARDT SUBROUTINE FOR NON-LINEAR LEAST
708 SQUARES.' Available at: https://www.osti.gov/biblio/4667484.

709 French, A. *et al.* (2008) 'Detecting land cover change at the Jornada Experimental Range, New
710 Mexico with ASTER emissivities', *Remote Sensing of Environment*, 112(4), pp. 1730–1748.
711 Available at: https://doi.org/10.1016/j.rse.2007.08.020.

712 Friedl, M.A. (2002) 'Forward and inverse modeling of land surface energy balance using surface
713 temperature measurements', *Remote Sensing of Environment*, 79(2–3), pp. 344–354. Available
714 at: https://doi.org/10.1016/S0034-4257(01)00284-X.

715 Ghent, D. *et al.* (2019) 'A New Approach to Defining Uncertainties for MODIS Land Surface
716 Temperature', *Remote Sensing*, 11(9), p. 1021. Available at: https://doi.org/10.3390/rs11091021.

717 Ghent, D.J. *et al.* (2017) 'Global Land Surface Temperature From the Along-Track Scanning
718 Radiometers: Global LST from the ATSRs', *Journal of Geophysical Research: Atmospheres*,
719 122(22), p. 12,167-12,193. Available at: https://doi.org/10.1002/2017JD027161.

720 Gillespie, A.R. *et al.* (1999) 'Temperature/emissivity separation algorithm theoretical basis
721 document, version 2.4', *ATBD contract NAS5-31372, NASA* [Preprint]. Available at:

http://crs.itb.ac.id/media/jurnal/refs/critical_review/Download/12Jun/atbd-ast-05-08.pdf (Accessed: 27 November 2013).

Goettsche, F. *et al.* (2013) 'Validation of Land Surface Temperature products in arid climate regions with permanent in-situ measurements', *AGU Fall Meeting Abstracts*, pp. GC43F-08.

Goettsche, F., Olesen, F. and Bork-Unkelbach, A. (2015) 'In-situ land surface emissivity retrieved from FTIR spectroscopic measurements at Gobabeb, Namibia', *EGU General Assembly Conference Abstracts*. (EGU General Assembly Conference Abstracts), p. 11402.

Göttsche, F.-M. *et al.* (2016) 'Long Term Validation of Land Surface Temperature Retrieved from MSG/SEVIRI with Continuous in-Situ Measurements in Africa', *Remote Sensing*, 8(5), p. 410. Available at: https://doi.org/10.3390/rs8050410.

Göttsche, F.-M. *et al.* (2017) *Report from the Field Inter- Comparison Experiment (FICE) for Land Surface Temperature*. OFE-D130-LST-FICE-report-V1-Iss-1-Ver-1. Karlsruhe Institute of Technology.

Göttsche, F.-M. and Hulley, G.C. (2012) 'Validation of six satellite-retrieved land surface emissivity products over two land cover types in a hyper-arid region', *Remote Sensing of Environment*, 124, pp. 149–158. Available at: https://doi.org/10.1016/j.rse.2012.05.010.

Hampel, F. (2014) 'Robust Inference', *Wiley StatsRef: Statistics Reference Online*. John Wiley & Sons, Ltd. Available at: https://doi.org/https://doi.org/10.1002/9781118445112.stat07417.

Hersbach, H. *et al.* (2023) *ERA5 hourly data on single levels from 1959 to present.* Copernicus Climate Change Service (C3S) Climate Data Store (CDS). Available at: 10.24381/cds.adbb2d47.

Hocking, J., Rayer, P. and Saunders, R. (2011) *RTTOV v10 Users Guide*. NWOSAF-MO-UD-023. EUMETSAT Satellite Application Facility on Numerical Weather Prediction.

Hook, S.J. (2017) *Combined ASTER and MODIS Emissivity database over Land (CAMEL) Emissivity Monthly Global 0.05Deg V002 [Data set]*. NASA EOSDIS Land Processes DAAC. Available at: https://doi.org/10.5067/MEaSUREs/LSTE/CAM5K30EM.002 (Accessed: 23 March 2023).

Hulley, G. *et al.* (2019) 'New ECOSTRESS and MODIS Land Surface Temperature Data Reveal Fine-Scale Heat Vulnerability in Cities: A Case Study for Los Angeles County, California', *Remote Sensing*, 11(18), p. 2136. Available at: https://doi.org/10.3390/rs11182136.

Hulley, G., Veraverbeke, S. and Hook, S. (2014) 'Thermal-based techniques for land cover change detection using a new dynamic MODIS multispectral emissivity product (MOD21)', *Remote Sensing of Environment*, 140, pp. 755–765. Available at: https://doi.org/10.1016/j.rse.2013.10.014.

Hulley, G.C., Hughes, C.G. and Hook, S.J. (2012) 'Quantifying uncertainties in land surface temperature and emissivity retrievals from ASTER and MODIS thermal infrared data: LST&E

UNCERTAINTIES', *Journal of Geophysical Research: Atmospheres*, 117(D23), p. n/a-n/a. Available at: https://doi.org/10.1029/2012JD018506.

Hussain, M. *et al.* (2013) 'Change detection from remotely sensed images: From pixel-based to object-based approaches', *ISPRS Journal of Photogrammetry and Remote Sensing*, 80, pp. 91–106. Available at: https://doi.org/10.1016/j.isprsjprs.2013.03.006.

Jimenez-Munoz, J.C. *et al.* (2009) 'Revision of the Single-Channel Algorithm for Land Surface Temperature Retrieval From Landsat Thermal-Infrared Data', *IEEE Transactions on Geoscience and Remote Sensing*, 47(1), pp. 339–349. Available at: https://doi.org/10.1109/TGRS.2008.2007125.

Jimenez-Munoz, J.C. *et al.* (2014) 'Land Surface Temperature Retrieval Methods From Landsat-8 Thermal Infrared Sensor Data', *IEEE Geoscience and Remote Sensing Letters*, 11(10), pp. 1840–1843. Available at: https://doi.org/10.1109/LGRS.2014.2312032.

Johannsen, F. *et al.* (2019) *Evaluation of skin temperature in ECMWF reanalyses*. Available at: https://doi.org/10.13140/RG.2.2.12405.01760.

Justice, C.O. *et al.* (1998) 'The Moderate Resolution Imaging Spectroradiometer (MODIS): land remote sensing for global change research', *IEEE Transactions on Geoscience and Remote Sensing*, 36(4), pp. 1228–1249. Available at: https://doi.org/10.1109/36.701075.

Kahya, O., Bayram, B. and Reis, S. (2010) 'Land cover classification with an expert system approach using Landsat ETM imagery: a case study of Trabzon', *Environmental Monitoring and Assessment*, 160(1–4), pp. 431–438. Available at: https://doi.org/10.1007/s10661-008-0707-6.

Kestens, Y. *et al.* (2011) 'Modelling the variation of land surface temperature as determinant of risk of heat-related health events', *International Journal of Health Geographics*, 10(1), p. 7. Available at: https://doi.org/10.1186/1476-072X-10-7.

Kotthaus, S. *et al.* (2014) 'Derivation of an urban materials spectral library through emittance and reflectance spectroscopy', *ISPRS Journal of Photogrammetry and Remote Sensing*, 94, pp. 194–212. Available at: https://doi.org/10.1016/j.isprsjprs.2014.05.005.

Langsdale, M.F. *et al.* (2020) 'Inter-Comparison of Field- and Laboratory-Derived Surface Emissivities of Natural and Manmade Materials in Support of Land Surface Temperature (LST) Remote Sensing', *Remote Sensing*, 12(24), p. 4127. Available at: https://doi.org/10.3390/rs12244127.

Langsdale, M.F. *et al.* (2021) 'Spectral Emissivity (SE) Measurement Uncertainties across 2.5–14 μm Derived from a Round-Robin Study Made across International Laboratories', *Remote Sensing*, 13(1), p. 102. Available at: https://doi.org/10.3390/rs13010102.

Levenberg, K. (1944) 'A Method for the Solution of Certain Non-Linear Problems in Least Squares', *Quarterly of Applied Mathematics*, 2(2), pp. 164–168.

Li, S. *et al.* (2014) ‘Evaluation of 10 year AQUA/MODIS land surface temperature with SURFRAD observations’, *International Journal of Remote Sensing*, 35(3), pp. 830–856. Available at: https://doi.org/10.1080/01431161.2013.873149.

Li, Z.-L. *et al.* (2023) ‘Satellite Remote Sensing of Global Land Surface Temperature: Definition, Methods, Products, and Applications’, *Reviews of Geophysics*, 61(1), p. e2022RG000777. Available at: https://doi.org/10.1029/2022RG000777.

Liu, Y. *et al.* (2019) ‘Enterprise LST Algorithm Development and Its Evaluation with NOAA 20 Data’, *Remote Sensing*, 11(17), p. 2003. Available at: https://doi.org/10.3390/rs11172003.

Luo, B. and Minnett, P.J. (2020) ‘Evaluation of the ERA5 Sea Surface Skin Temperature with Remotely-Sensed Shipborne Marine-Atmospheric Emitted Radiance Interferometer Data’, *Remote Sensing*, 12(11), p. 1873. Available at: https://doi.org/10.3390/rs12111873.

MacCallum, S.N. and Merchant, C.J. (2012) ‘Surface water temperature observations of large lakes by optimal estimation’, *Canadian Journal of Remote Sensing*, 38(1), pp. 25–45. Available at: https://doi.org/10.5589/m12-010.

Marquardt, D.W. (1963) ‘An Algorithm for Least-Squares Estimation of Nonlinear Parameters’, *Journal of the Society for Industrial and Applied Mathematics*, 11(2), pp. 431–441.

Masiello, G. *et al.* (2018) ‘Physical Retrieval of Land Surface Emissivity Spectra from Hyper-Spectral Infrared Observations and Validation with In Situ Measurements’, *Remote Sensing*, 10(6), p. 976. Available at: https://doi.org/10.3390/rs10060976.

Masiello, G. and Serio, C. (2013) ‘Simultaneous physical retrieval of surface emissivity spectrum and atmospheric parameters from infrared atmospheric sounder interferometer spectral radiances’, *Applied Optics*, 52(11), p. 2428. Available at: https://doi.org/10.1364/AO.52.002428.

Matsumoto-Moriyama, M. and Arai, K. (1994) ‘An inversion for emissivity - temperature separation with aster data’, *Advances in Space Research*, 14(3), pp. 67–70. Available at: https://doi.org/10.1016/0273-1177(94)90194-5.

Meerdink, S.K. *et al.* (2019) ‘The ECOSTRESS spectral library version 1.0’, *Remote Sensing of Environment*, 230, p. 111196. Available at: https://doi.org/10.1016/j.rse.2019.05.015.

Merchant, C.J. *et al.* (2008) ‘Optimal estimation of sea surface temperature from split-window observations’, *Remote Sensing of Environment*, 112(5), pp. 2469–2484. Available at: https://doi.org/10.1016/j.rse.2007.11.011.

Merchant, C.J. *et al.* (2009) ‘Sea surface temperature from a geostationary satellite by optimal estimation’, *Remote Sensing of Environment*, 113(2), pp. 445–457. Available at: https://doi.org/10.1016/j.rse.2008.10.012.

Merchant, C.J., Saux-Picart, S. and Waller, J. (2020) ‘Bias correction and covariance parameters for optimal estimation by exploiting matched in-situ references’, *Remote Sensing of Environment*, 237, p. 111590. Available at: https://doi.org/10.1016/j.rse.2019.111590.

NASA (2024) *Welcome to Surface Biology and Geology study — Surface Biology and Geology*. Available at: https://sbg.jpl.nasa.gov/ (Accessed: 2 April 2024).

Nielsen-Englyst, P. *et al.* (2018) 'Optimal Estimation of Sea Surface Temperature from AMSR-E', *Remote Sensing*, 10(2), p. 229. Available at: https://doi.org/10.3390/rs10020229.

Organization (WMO), W.M. *et al.* (2022) *GCOS, 245. The 2022 GCOS ECVs Requirements (GCOS 245)*. Geneva: WMO.

Perry, M. (2024) 'A new inverse method for the retrieval of Land Surface Temperature and Emissivity from the ASTER instrument'. Zenodo. Available at: https://doi.org/10.5281/zenodo.10964925.

Prata, D.F. (2002) 'Land Surface Temperature Measurement from Space: AATSR Algorithm Theoretical Basis Document'.

Press, W.H. *et al.* (2007) *Numerical Recipes 3rd Edition: The Art of Scientific Computing*. 3rd edn. USA: Cambridge University Press.

Rangisetty, A. *et al.* (2020) *Application of ECOSTRESS multispectral LWIR images to assess topsoil properties: preliminary results on agricultural test sites in Central Italy*. EGU2020-5319. Copernicus Meetings. Available at: https://doi.org/10.5194/egusphere-egu2020-5319.

Ridd, M.K. and Liu, J. (1998) 'A Comparison of Four Algorithms for Change Detection in an Urban Environment', *Remote Sensing of Environment*, 63(2), pp. 95–100. Available at: https://doi.org/10.1016/S0034-4257(97)00112-0.

Rodgers, Clive.D. (2000) *Inverse Methods for Atmospheric Sounding*. World Scientific (Series on Atmospheric, Oceanic and Planetary Physics).

Román, M.O. *et al.* (2024) 'Continuity between NASA MODIS Collection 6.1 and VIIRS Collection 2 land products', *Remote Sensing of Environment*, 302, p. 113963. Available at: https://doi.org/10.1016/j.rse.2023.113963.

Shi, J. and Hu, C. (2021) 'Evaluation of ECOSTRESS Thermal Data over South Florida Estuaries', *Sensors (Basel, Switzerland)*, 21(13), p. 4341. Available at: https://doi.org/10.3390/s21134341.

Sobrino, J.A. *et al.* (2016) 'Synergistic use of MERIS and AATSR as a proxy for estimating Land Surface Temperature from Sentinel-3 data', *Remote Sensing of Environment*, 179, pp. 149–161. Available at: https://doi.org/10.1016/j.rse.2016.03.035.

Voogt, J.A. and Oke, T.R. (2003) 'Thermal remote sensing of urban climates', *Remote Sensing of Environment*, 86(3), pp. 370–384. Available at: https://doi.org/10.1016/S0034-4257(03)00079-8.

Wang, W., Liang, S. and Meyers, T. (2008) 'Validating MODIS land surface temperature products using long-term nighttime ground measurements', *Remote Sensing of Environment*, 112(3), pp. 623–635. Available at: https://doi.org/10.1016/j.rse.2007.05.024.

Xue, J. *et al.* (2020) 'Sharpening ECOSTRESS and VIIRS land surface temperature using harmonized Landsat-Sentinel surface reflectances', *Remote sensing of environment*, 251, p. 112055. Available at: https://doi.org/10.1016/j.rse.2020.112055.

Yamaguchi, Y. *et al.* (1998) 'Overview of Advanced Spaceborne Thermal Emission and Reflection Radiometer (ASTER)', *IEEE Transactions on Geoscience and Remote Sensing*, 36(4), pp. 1062–1071. Available at: https://doi.org/10.1109/36.700991.

Yu, Y. *et al.* (2012) 'Validation of GOES-R Satellite Land Surface Temperature Algorithm Using SURFRAD Ground Measurements and Statistical Estimates of Error Properties', *IEEE Transactions on Geoscience and Remote Sensing*, 50(3), pp. 704–713. Available at: https://doi.org/10.1109/TGRS.2011.2162338.

Yuan, F. and Bauer, M.E. (2007) 'Comparison of impervious surface area and normalized difference vegetation index as indicators of surface urban heat island effects in Landsat imagery', *Remote Sensing of Environment*, 106(3), pp. 375–386. Available at: https://doi.org/10.1016/j.rse.2006.09.003.

Zhengming Wan and Dozier, J. (1996) 'A generalized split-window algorithm for retrieving land-surface temperature from space', *IEEE Transactions on Geoscience and Remote Sensing*, 34(4), pp. 892–905. Available at: https://doi.org/10.1109/36.508406.